Quarterly Technical Report
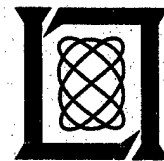
Solid State Research

1998:4

Lincoln Laboratory

MASSACHUSETTS INSTITUTE OF TECHNOLOGY

LEXINGTON, MASSACHUSETTS

19990330 115

This report is based on studies performed at Lincoln Laboratory, a center for research operated by Massachusetts Institute of Technology. The work was sponsored by the Department of the Air Force under Contract F19628-95-C-0002.

This report may be reproduced to satisfy needs of U.S. Government agencies.

The ESC Public Affairs Office has reviewed this report, and it is releasable to the National Technical Information Service, where it will be available to the general public, including foreign nationals.

This technical report has been reviewed and is approved for publication.

FOR THE COMMANDER

Gary Tutungian
Administrative Contracting Officer
Contracted Support Management

MASSACHUSETTS INSTITUTE OF TECHNOLOGY
LINCOLN LABORATORY

SOLID STATE RESEARCH

QUARTERLY TECHNICAL REPORT

1 AUGUST – 31 OCTOBER 1998

ISSUED 23 MARCH 1999

LEXINGTON   MASSACHUSETTS

ABSTRACT

This report covers in detail the research work of the Solid State Division at Lincoln Laboratory for the period 1 August through 31 October 1998. The topics covered are Quantum Electronics, Electro-optical Materials and Devices, Submicrometer Technology, Biosensor and Molecular Technologies, Microelectronics, Analog Device Technology, and Advanced Silicon Technology. Funding is provided by several DoD organizations—including the Air Force, Army, BMDO, DARPA, Navy, NSA, and OSD—and also by the DOE, NASA, and NIST.

TABLE OF CONTENTS

TABLE OF CONTENTS (Continued)

LIST OF ILLUSTRATIONS

LIST OF ILLUSTRATIONS (Continued)

LIST OF ILLUSTRATIONS (Continued)

LIST OF ILLUSTRATIONS (Continued)

LIST OF TABLES

INTRODUCTION

1. QUANTUM ELECTRONICS

The thermal expansion coefficient and *dn/dT* have been measured in undoped YAG below 300 K using interferometry techniques. The thermal expansion coefficient at 125 K was 2.70×10^{-6} K^{-1} and *dn/dT* at 633 nm was 2.5×10^{-6} K^{-1}, compared with 7×10^{-6} K^{-1} and 9×10^{-6} K^{-1} for these quantities at 300 K.

2. ELECTRO-OPTICAL MATERIALS AND DEVICES

A ring laser using a tapered GaInAsP/InP amplifier as the gain element has provided 80-mW single-frequency output in a single-mode fiber. The fiber ring contains a tunable Fabry-Perot filter and a fiber Bragg grating to select a single mode of the ring.

The suitability of the wavelength range provided by silicon photodiode detector arrays for monitoring the spectral reflectance during epitaxial growth of GaSb, AlGaAsSb, and GaInAsSb has been demonstrated. By using a virtual interface model, the growth rate and complex refractive index at the growth temperature have been extracted for these alloys over the 600–1000-nm spectral range.

The optical characteristics of epitaxial GaInAsSb, a material for thermophotovoltaics, have been evaluated by photoluminescence. For these layers grown lattice matched to GaSb substrates by organometallic vapor phase epitaxy, the optical quality is improved as the growth temperature is lowered from 575 to 525°C.

3. SUBMICROMETER TECHNOLOGY

The chemical components released during 193-nm-wavelength exposure of photoresists have been analyzed, and a model has been developed to predict the effects of these chemicals on optical elements. This technique has been used to compare the long-term effects of using various resists in an optical exposure system.

4. BIOSENSOR AND MOLECULAR TECHNOLOGIES

A novel sensor is being developed which uses live cells integrated with microelectronics in order to identify pathogenic bacteria and viruses in a rapid, sensitive fashion. The feasibility of this approach has been proven by creating suitable genetically engineered cells, by demonstrating that their responses are very fast, sensitive, and specific, and by fabricating prototype hardware for the sensor.

5. MICROELECTRONICS

Attempts have been made to deform imager arrays to take advantage of the improved optical response of a curved focal surface compared to a planar one. A petal chip approach has been used to successfully deform a thinned Si membrane to a spherical surface with a 39-mm radius of curvature.

6. ANALOG DEVICE TECHNOLOGY

The energy sensitivity S_e of a superconductive comparator has been measured to be about 1500 h (Planck's constant) when the comparator was clocked at 40 MHz, and the noise floor was low enough that we could observe excess low-frequency noise below 5 Hz. If we clock the comparator into the gigahertz range, it may be possible to operate it with $S_e = h$, the energy uncertainty principle limit.

7. ADVANCED SILICON TECHNOLOGY

The high-frequency performance of 0.25-μm channel length n- and p-channel metal-oxide semiconductor field-effect transistors (MOSFETs), developed as part of Lincoln Laboratory's fully depleted silicon-on-insulator CMOS process technology, has been investigated. F_t's near 30 GHz and F_{max}'s from 30 to 40 GHz have been obtained for n-channel devices, while F_t and F_{max} were 13 and 20 GHz, respectively, for the p-channel MOSFETs.

REPORTS ON SOLID STATE RESEARCH

1 AUGUST THROUGH 31 OCTOBER 1998

PUBLICATIONS

Silicon-Rich-Methacrylate Bilayer Resist for 193-nm Lithography	A. J. Blakeney[*] A. H. Gabor[*] D. White[*] T. Sternhäsler[*] W. R. Deady J. J. Jarmalowicz R. R. Kunz K. R. Dean[*] G. K. Rich[*] D. Shark[*]	*Solid State Technol.* **41**(6), 69 (1998)
Terahertz Photomixing in Low-Temperature-Grown GaAs	E. R. Brown S. Verghese K. A. McIntosh	*Proc. SPIE* **3357**, 132 (1998)
Low-Loss High-Efficiency and High-Power Diode-Pumped Mid-Infrared GaInSb/InAs Quantum Well Lasers	H. Q. Le C. H. Lin[*] S. S. Pei[*]	*Appl. Phys. Lett.* **72**, 3434 (1998)

ACCEPTED FOR PUBLICATION

Growth and Morphology of Er-Doped GaN on Sapphire and HVPE Substrates	R. J. Molnar R. Birkhahn[*] R. Hudgins[*] D. Lee[*] A. J. Steckl[*] J. M. Zavada[*]	*J. Vac. Sci. Technol.*

---

[*]Author not at Lincoln Laboratory.

Annealing Studies on GaN Hydride Vapor Phase Epitaxial Layers	R. J. Molnar D. C. Reynolds[*] D. C. Look[*] T. Wille K. K. Bajaj T. C. Collins	*Appl. Phys. Lett.*
Approaches to Designing Thermally Stable Schottky Contacts to *n*-GaN	R. J. Molnar H. S. Venugopalan[*] S. E. Mohney[*] J. M. DeLucca[*]	*Semicond. Sci. Technol.*
Rapid Evaluation of Dislocation Density in *n*-type GaN Films Using Photoenhanced Wet Etching	R. J. Molnar C. Youtsey[*] I. Adesida[*] L. T. Romano[*]	*Appl. Phys. Lett.*
A Photomixer Local Oscillator for a 630 GHz Heterodyne Receiver	S. Verghese K. A. McIntosh S. M. Duffy S. D. Calawa E. K. Duerr[*] D-Y. E. Tong[*] R. Kimberk[*] R. Blundell[*]	*Appl. Phys. Lett.*
InAs Doped Silica Films for Saturable Absorber Applications	J. N. Walpole L. J. Missaggia I. P. Bilinsky[*] J. G. Fujimoto[*]	*Appl. Phys. Lett.*

---

[*]Author not at Lincoln Laboratory.

PRESENTATIONS[†]

Photonic A/D Converters for Wideband and High Dynamic Range Performance	J. C. Twichell Z. J. Lemnios C. Dickerson[*]	7th Annual AIAA/BMDO Technical Readiness Conference, Colorado Springs, Colorado, 3-7 August 1998
Transmit Filters for Wireless Basestations	A. C. Anderson H. Wu[*] Z. Ma[*] P. A. Polakos[*] P. M. Mankiewich[*] T. Kaplan[*] A. Barfknecht[*]	
Low-T_c Superconductive Circuits Fabricated on 150-mm Diameter Wafers by Using a Doubly Planarized Nb/AlO$_x$/Nb Process	K. K. Berggren D. A. Feld J. P. Sage E. M. Macedo	Applied Superconductivity Conference, Palm Desert, California, 13-18 September 1998
Evaluation of Electrical Characteristics of Nb/Al/AlO$_x$/Nb Josephson Junctions Using Test Structures at 300 K	K. K. Berggren J. P. Sage A. H. Worsham[*] M. O'Hara[*]	
Measurements of the Energy Sensitivity of a Superconductive Comparator	D. A. Feld J. P. Sage K. K. Berggren A. Siddiqui[*]	
Magnetically Tunable Superconducting Resonators and Filters	D. E. Oates G. F. Dionne	

---

[*]Author not at Lincoln Laboratory.

[†]Titles of presentations are listed for information only. No copies are available for distribution.

Measurements and Modeling of Microwave Impedance High-T_c Grain Boundaries	D. E. Oates Y. M. Habib[*] C. J. Lehner[*] L. R. Vale[*] R. H. Ono[*] G. Dresselhaus[*] M. Dresselhaus[*]	Applied Superconductivity Conference, Palm Desert, California, 13-18 September 1998
First Demonstration of Correlation in a Niobum Superconductive Programmable Binary-Analog Matched Filter	J. P. Sage D. A. Feld	
Passively Q-Switched Microchip Lasers and Applications	J. J. Zayhowski	European Conference on Lasers and Electro-Optics/ European Quantum Electronics Conference, Glasgow, Scotland, 13-18 September 1998
Dose Control Errors from Transient Absorption in Fused Silica	A. Grenville V. Liberman M. Rothschild J. H. C. Sedlacek A. K. Bates	4th International Symposium on 193-nm Lithography, Tyrol, Austria, 14-17 September 1998
Photoresist Outgassing at 193 nm	R. R. Kunz D. K. Downs	
Damage Assessment of Optical Materials after Long-Term Irradiation	V. Liberman M. Rothschild J. H. C. Sedlacek R. S. Uttaro	

---

[*]Author not at Lincoln Laboratory.

Antimonide-Based Diode and Optically Pumped Mid-Infrared Lasers	H. K. Choi G. W. Turner H. Q. Le J. N. Walpole M. J. Manfra M. K. Connors L. J. Missaggia	Workshop on Middle Infrared Coherent Sources, Corsica, France, 22-26 September 1998
Marathon Testing of Optical Materials for 193-nm Lithographic Applications	V. Liberman M. Rothschild J. H. C. Sedlacek R. S. Uttaro A. K. Bates C. VanPeski	Annual Symposium on Optical Materials for High-Power Lasers, Boulder, Colorado, 28 September–2 October 1998
Current Status of Mid-Infrared Semiconductor Lasers	H. K. Choi	Optical Society of America Annual Meeting, Baltimore, Maryland, 4–9 October 1998
Extending the Cutoff Wavelength of Lattice-Matched GaInAsSb/GaSb Thermophotovoltaic Devices	C. A. Wang D. C. Oakley H. K. Choi	4th National Renewable Energy Laboratory Conference on Thermo-photovoltaic Generation of Electricity, Denver, Colorado, 11-14 October 1998
A Deep Submicrometer Fully-Depleted Low Power SOI CMOS Process Technology	J. A. Burns	Lincoln Laboratory Technical Seminar Series, University of Michigan, Ann Arbor, Michigan, 30 October 1998

ORGANIZATION

SOLID STATE DIVISION

D. C. Shaver, *Head*
R. W. Ralston, *Associate Head*
N. L. DeMeo, Jr., *Assistant*
Z. J. Lemnios, *Senior Staff*

J. W. Caunt, *Assistant Staff*
K. J. Challberg, *Administrative Staff*
J. D. Pendergast, *Administrative Staff*

SUBMICROMETER TECHNOLOGY

M. Rothschild, *Leader*
T. M. Lyszczarz, *Assistant Leader*
T. H. Fedynyshyn, *Senior Staff*
R. R. Kunz, *Senior Staff*

Astolfi, D. K.	Goodman, R. B.
Bloomstein, T. M.	Krohn, K. E.
Craig, D. M.	Liberman, V.
DiNatale, W. F.	Maki, P. A.
Doran, S. P.	Palmacci, S. T.
Efremow, N. N., Jr.	Palmateer, S. C.
Forte, A. R.	Sedlacek, J. H. C.
Geis, M. W.	Uttaro, R. S.

QUANTUM ELECTRONICS

A. Sanchez-Rubio, *Leader*
T. Y. Fan, *Assistant Leader*
T. H. Jeys, *Senior Staff*

Aggarwal, R. L.	DiCecca, S.
Buchter, S.	Dill, C., III
Cook, C. C.	Le, H. Q.
Daneu, J. L.	Ochoa, J. R.
Daneu, V.	Zayhowski, J. J.

ELECTRO-OPTICAL MATERIALS AND DEVICES

D. L. Spears, *Leader*
J. C. Twichell, *Assistant Leader*
H. K. Choi, *Senior Staff*
R. C. Williamson, *Senior Staff*

Bailey, R. J.	Harris, C. T.	Oakley, D. C.
Betts, G. E.	Liau, Z. L.	O'Donnell, F. J.
Calawa, A. R.*	Lightfoot, A.	Oswald, J.[†]
Calawa, D. R.	Mahoney, L. J.	Poillucci, R. J.
Calawa, S. D.	Manfra, M. J.	Reeder, R. E.
Choi, S. S.[†]	McIntosh, K. A.	Taylor, P. J.
Connors, M. K.	Missaggia, L. J.	Turner, G. W.
Cronin, S.[†]	Molnar, R. J.	Verghese, S.
Donnelly, J. P.	Mull, D. E.	Vineis, C. J.[†]
Duerr, E.[†]	Napoleone, A.	Walpole, J. N.
Goodhue, W. D.	Nee, P.[†]	Wang, C. A.
Harman, T. C.	Nitishin, P. M.	Wasserman, J.

*Part Time
[†]Research Assistant

xix

xx

1. QUANTUM ELECTRONICS

1.1 THERMAL COEFFICIENTS OF THE EXPANSION AND REFRACTIVE INDEX IN YAG

Yb:YAG lasers operating at cryogenic temperatures (~100 K) have been shown to have substantially reduced thermooptic effects compared with Nd:YAG lasers operating at 300 K with the same average power [1]. This reduction in thermooptic effects is in part due to higher thermal conductivity, lower thermal expansion, and smaller dn/dT of YAG at lower temperature. In order to make accurate projections of the thermooptic effects at cryogenic temperatures, accurate values for thermal expansion coefficient and dn/dT are needed. The thermal expansion coefficient α, defined as $(1/L)dL/dT$, in YAG was previously determined for temperatures less than 300 K from x-ray measurements of the lattice constant [2], and this data was limited in its sensitivity. We have performed thermal expansion measurements using an interferometer in the range 125–266 K to provide improved low-temperature data.

We have used the method of Foster and Osterink [3] to make our thermal expansion measurements. Undoped YAG flats are bonded to the ends of a 15.01-mm-long piece of undoped YAG to form a Fizeau interferometer. The sample is placed in a vacuum dewar to allow cooling. The undoped YAG flats are illuminated by a He-Ne laser operating at 543 nm, and the intensity of the reflected fringes are recorded as the temperature is varied. Table 1-1 shows the measured thermal expansion coefficient with the estimated error in the measurements being no more than $\pm 0.2 \times 10^{-6}$ K^{-1}. The error is dominated by error in the temperature measurement. The temperature is not varied at the same rate over the entire temperature range, which leads to a small, and slightly varying, lag between the actual temperature of the YAG sample and the measured temperature at the sensor.

TABLE 1-1
Measured Values for $\alpha(T)$

Temperature (K)	α (in 10^{-6}K^{-1})
125	2.70
156	3.37
176	3.97
216	4.75
236	5.34
266	6.01

We have fitted the tabulated values from Table 1-1 to a functional form of

$$\alpha(T) = aT + bT^2 + cT^3 \tag{1.1}$$

and found that $a = 1.9998 \times 10^{-8}$ K^{-2}, $b = 1.56101 \times 10^{-11}$ K^{-3}, and $c = 2.19111 \times 10^{-14}$ K^{-4}. There is no fundamental relationship available for the functional dependence between lattice constant and temperature, and consequently the polynomial form of Equation (1.1) was chosen because, first, it gives $\alpha(0) = 0$ as expected and, second, because α is nearly linear over the temperature range of our measurements. Figure 1-1 shows our experimental data points and the fit of Equation (1.1). The fit gives reasonable agreement with other experimental data around 300 K. While our experimental measurements were done only to a lowest temperature of 125 K, the fit should give a reasonable estimate for temperatures below 125 K because α is only a slowly varying function and because the fit does give the proper value of α at $T = 0$. Above about 300 K, the fit is not expected to be good because the slope of $\alpha(T)$ changes substantially for $T > 300$ K [4].

With this improved thermal expansion data, we have recalculated dn/dT at 633 nm using the change in optical path length data from [5]. The optical path length is given by nL where n is the refractive index of the material and L is its physical length. The change in refractive index with temperature, dn/dT, can be calculated from the change in optical path length with temperature and α using
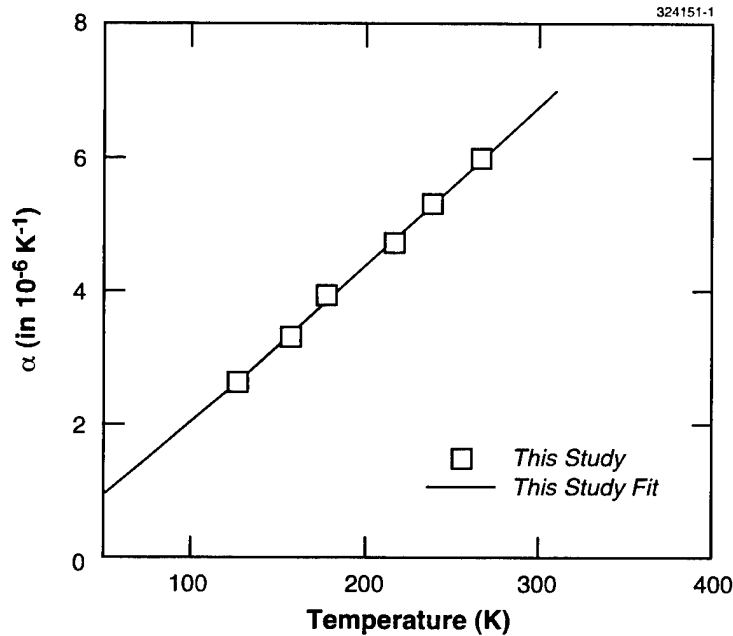
Figure 1-1. α for YAG. Open squares are for data of this measurement and the solid line is the fit of Equation (1.1).

2
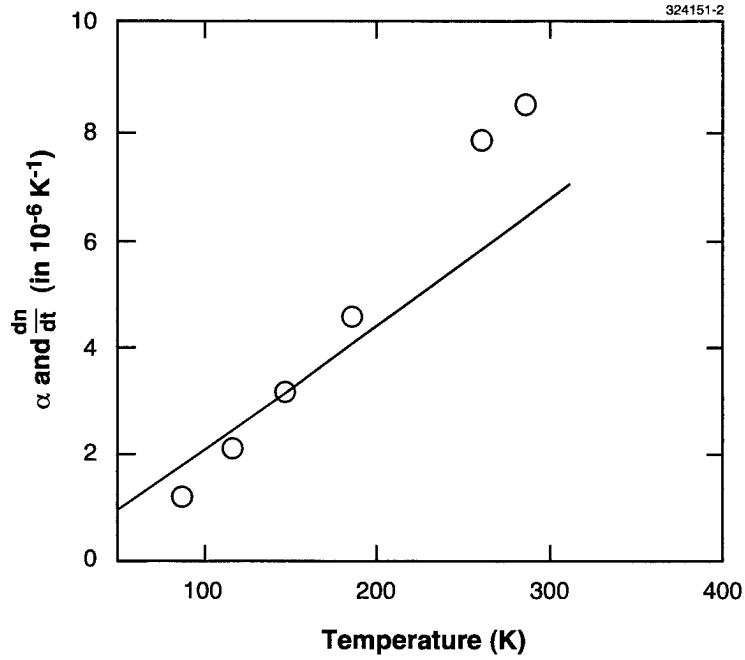
Figure 1-2. dn/dT at 633 nm and fit of α for YAG. The open circles are data calculated using the experimental data from [5] of optical path length change with temperature at 633 nm and the solid line is the fit for α from Equation (1.1).

$$\frac{1}{nL}\frac{d(nL)}{dT} = \frac{1}{n}\frac{dn}{dt} + \alpha \quad . \tag{1.2}$$

This revised *dn/dT* data are shown in Figure 1-2 along with the fit for α. The *dn/dT* drops from approximately 9×10^{-6} K^{-1} at 300 K to about 1.5×10^{-6} K^{-1} at 100 K, indicating that thermal lensing and higher-order thermal distortions should be substantially reduced in cryogenically cooled YAG lasers, as is observed.

R. Wynne
J. L. Daneu
T. Y. Fan

3

REFERENCES

1. T. Y. Fan, T. Crow, and B. Hoden, *Proc. SPIE* **3381**, 200 (1998).

2. P. H. Klein and W. J. Croft, *J. Appl. Phys.* **38**, 1603 (1967).

3. J. D. Foster and L. M. Osterink, *Appl. Opt.* **7**, 2428 (1968).

4. K. L. Ovanesyan, A. G. Petrosyan, G. O. Shirinyan, and A. A. Avetisyan, *Inorg. Mater.* **17**, 308 (1981).

5. T. Y. Fan and J. Daneu, *Appl. Opt.* **37**, 1635 (1998).

2. ELECTRO-OPTICAL MATERIALS AND DEVICES

2.1 TUNABLE 1.3-μm FIBER RING LASER EMPLOYING A TAPERED DIODE AMPLIFIER

Tapered diode lasers and amplifiers have demonstrated a combination of high power and near-diffraction-limited beams which make these devices attractive for use as high-brightness sources at a variety of wavelengths, including 1.3 μm [1]. When operated as an amplifier fed by a lower-power laser with low relative intensity noise (RIN), the output of a 1.3-μm tapered amplifier has a desirable combination of high power, high brightness, and low RIN [2]. However, when tapered 1.3-μm devices have facets coated to operate as stand-alone laser sources, the spectral purity and RIN have generally been poor. By operating a tapered amplifier in a ring, a stand-alone source is obtained which retains the excellent properties of the output of a tapered amplifier. Further, narrow linewidth and the ability to tune the ring laser open up a wide range of applications. A ring laser employing a tapered amplifier [3] and polarization tuning of a low-power fiber ring laser containing a semiconductor optical amplifier have been demonstrated [4].

The 1.3-μm tapered amplifier is a three-quantum-well separate confinement heterostructure with a ridge-waveguide input section and a 210-μm-wide output aperture. Both facets are antireflection coated. The configuration of the ring laser is shown in Figure 2-1. All components, with the exception of the fiber containing the fiber Bragg grating (FBG), are polarization preserving. A launcher incorporating an isolator couples an optical wave into the ridge-waveguide end of a tapered amplifier. The output of the tapered amplifier passes through a cylindrical lens, a circular lens, and an isolator to form a circular beam which is coupled, at approximately 43% efficiency, into a single-mode fiber. A fiber splitter couples 16% of the power into the fiber ring and 60% of the power to the output. The FBG filter consists of a three-port circulator with a reflective 0.1-nm full width at half-maximum (FWHM) (17 GHz) apodized FBG with a center wavelength of 1325 nm on the middle port. Finer filtering in the ring is provided by a tunable Fabry-Perot (FP) filter with 50-MHz resolution and 10-GHz free spectral range. The fiber pigtails on the various components dominate the length of the ring and yield a ring-mode spacing of about 50 MHz.
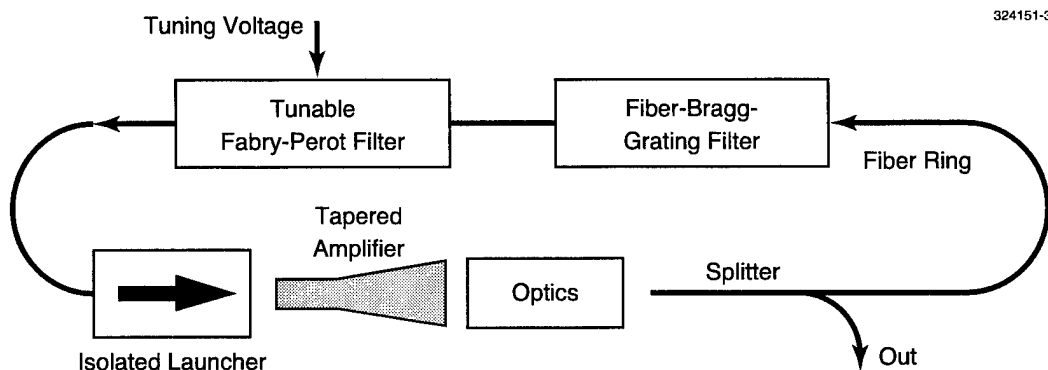
Figure 2-1. Fiber ring laser configuration.

5

324151-4P
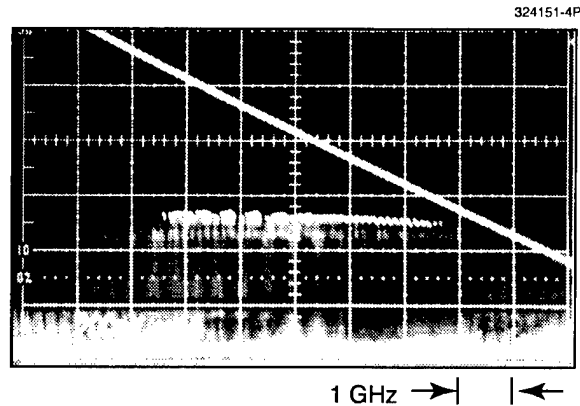
1 GHz →| |←

Figure 2-2. Fabry-Perot (FP) tuning voltage (2 V/div) and ring-laser output power vs Fabry-Perot tuning. Horizontal scale = 1 GHz/div.

324151-5P
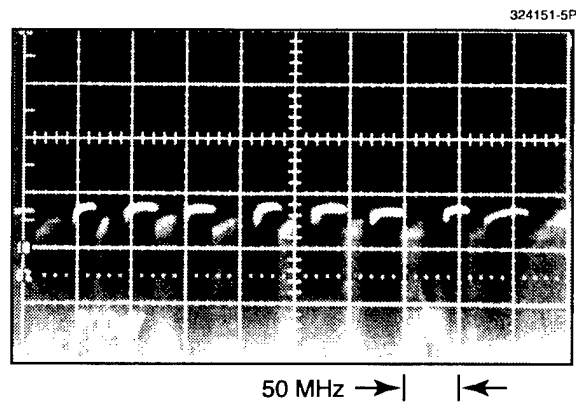
50 MHz →| |←

Figure 2-3. Ring-laser output power vs FP tuning. Horizontal scale = 50 MHz/div.

Figure 2-2 shows the output power of the ring and the tuning voltage applied to the FP. In the center of the figure, one passband of the FP is near the center of the FBG passband. In this region, stable ring oscillation can be achieved. When the FP is tuned so that two FP passbands of about equal amplitude fall within the FBG passband, chaotic operation occurs and power drops as seen on the left and right sides of Figure 2-2. Figure 2-3 shows the optical output power as a function of FP tuning voltage when a single FP passband is located near the center of the FBG passband. The response shows nearly flat output when one cavity mode is nearly centered on the FP passband. When the FP is tuned so that the filter straddles two cavity modes, the power drops as seen between the flat-topped regions of Figure 2-3. The FP filter can be tuned to select one of the cavity modes. However, no precautions were taken to mechanically or thermally stabilize the fiber in the ring. As a consequence, the cavity modes drift around. In order to stay locked on a

6

single cavity mode, a small dither is applied to the FP voltage and a feedback loop keeps the FP centered on a single cavity mode. A tuning range wider than the width of the FBG is potentially possible by stress tuning the FBG wavelength.

When operated in the ring, the maximum power out of the tapered laser was about 300 mW at a current of 3.5 A. The power coupled to the output port was 80 mW. Output powers higher than this are potentially possible by changing the ratio in the splitter, by using more efficient optics, and by employing higher-power tapered amplifiers. Tapered lasers with 1-W output at the facet at 1.3 μm have been demonstrated. The output power vs input power characteristics of the tapered amplifier within the ring were measured by introducing a calibrated attenuation within the ring by rotating a half-wave plate in the output optics. The loss of the passive components was calibrated so that the power at any point in the ring could be calculated from the output power. For stable operation the tapered amplifier was operated in the saturated region. Operation with nearly constant output power was achieved over an approximately 10-dB range of attenuation in the ring. With higher levels of attenuation, the input-output characteristic became more linear and the ring laser dropped in and out of oscillation with only minor changes in optical alignment. This is to be expected for a ring with a gain element operating nearly linearly. When the amplifier is operating in saturation, a low RIN of −153 to −161 dB/Hz was measured in the range 0.01–20 GHz.

R. C. Williamson   G. E. Betts
J. P. Donnelly   S. H. Groves
J. N. Walpole   F. J. O'Donnell
R. J. Bailey

2.2   IN-SITU MONITORING OF GaSb, GaInAsSb, AND AlGaAsSb

In-situ optical monitoring during organometallic vapor phase epitaxy (OMVPE) provides insight into complex growth processes and has led to improvements in the growth process and the resulting materials [5]. Near-normal spectral reflectance is a particularly attractive technique for in-situ monitoring, because it can provide real-time information on the growth rate and complex refractive index of each thin film layer and can be quickly analyzed for closed-loop process control [6]. In addition, it is less expensive and easier to implement than most other in-situ process monitors. Here, we demonstrate the usefulness of a conventional Si photodiode array (PDA) for monitoring in situ the growth of III-V antimonide-based materials. The growth rates and optical constants of GaSb, AlGaAsSb, and GaInAsSb are determined from the spectral reflectance. Extracted growth rates compare favorably with layer thicknesses determined ex situ using high resolution x-ray diffraction (HRXRD).

Figure 2-4 shows a schematic diagram of the experimental setup. Optical fibers and various mirrors and lenses are used to direct white light from a 5-W tungsten halogen lamp to the vertical rotating-disk reactor, and the reflected signal to the Si PDA spectrometer, which interfaces directly to the computer. The Si spectrometer is a commercial 512-element array with a dispersive element and has a wavelength range

324151-6

Lamp   Mirrors

Lens

Spectrometer

Computer

Vertical Rotating Disk Reactor
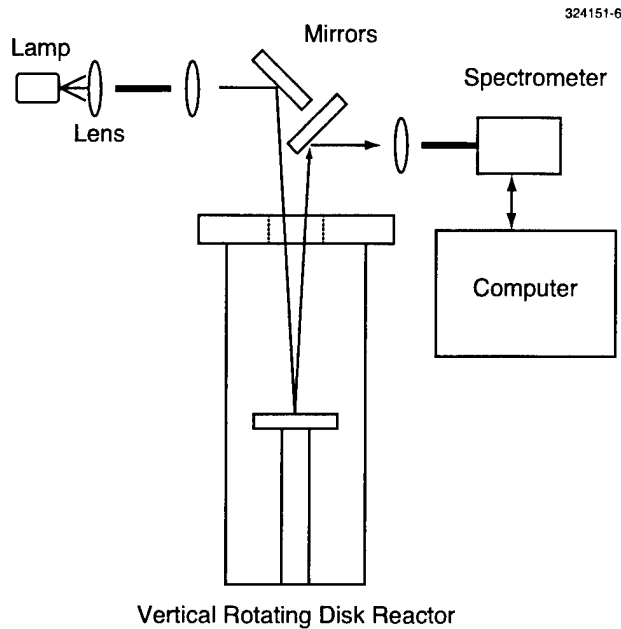
Figure 2-4. Schematic diagram of experimental setup for in-situ process monitoring using near-normal spectral reflectance.

of 380–1100 nm with a 2.6-nm spectral resolution. Calibration of the spectrometer to provide absolute reflectance values was accomplished by referencing the raw counts of a silver mirror to the mirror's absolute spectral reflectance. The spectral reflectance as a function of growth time was acquired via a Windows-based program and stored to disk. Quantitative analysis of the reflectance was performed using a virtual-interface (VI) model [7] to yield the growth rate and complex refractive index.

GaSb, $Ga_{0.83}In_{0.17}As_{0.16}Sb_{0.84}$, and $Al_{0.2}Ga_{0.8}As_{0.02}Sb_{0.98}$ epilayers with 25°C cutoff wavelength $\lambda \sim$ 1.7, 2.3, and 1.2 μm, respectively, were grown lattice matched to GaSb in a vertical rotating-disk reactor with H_2 carrier gas at a flow rate of 10 slpm and reactor pressure of 150 Torr, as described previously [8]. Triethylgallium, trimethylindium, tritertiarybutylaluminum, trimethylantimony, and tertiarybutylarsine were used as precursors. Layers were grown at 525 or 550°C on Te-doped GaSb, (100) misoriented 6° toward (111)B. Epilayer composition was determined from HRXRD splitting of ω-2Θ scans, the peak emission in 300-K photoluminescence spectra, and the energy gap dependence on composition. Epitaxial layer thickness was determined within ±5% by HRXRD, using software based on the Taupin-Tagachi solution to dynamical x-ray diffraction.

Reflectance at 650, 800, and 1000 nm as a function of time is shown in Figure 2-5. The initial 600 s corresponds to heatup of the GaSb substrate from 25 to 525°C, shown in Figures 2-5(a) and 2-5(c), or to 550°C, shown in Figure 2-5(b). It is evident from Figures 2-5(a) and 2-5(c) that the reflectance signal dur-
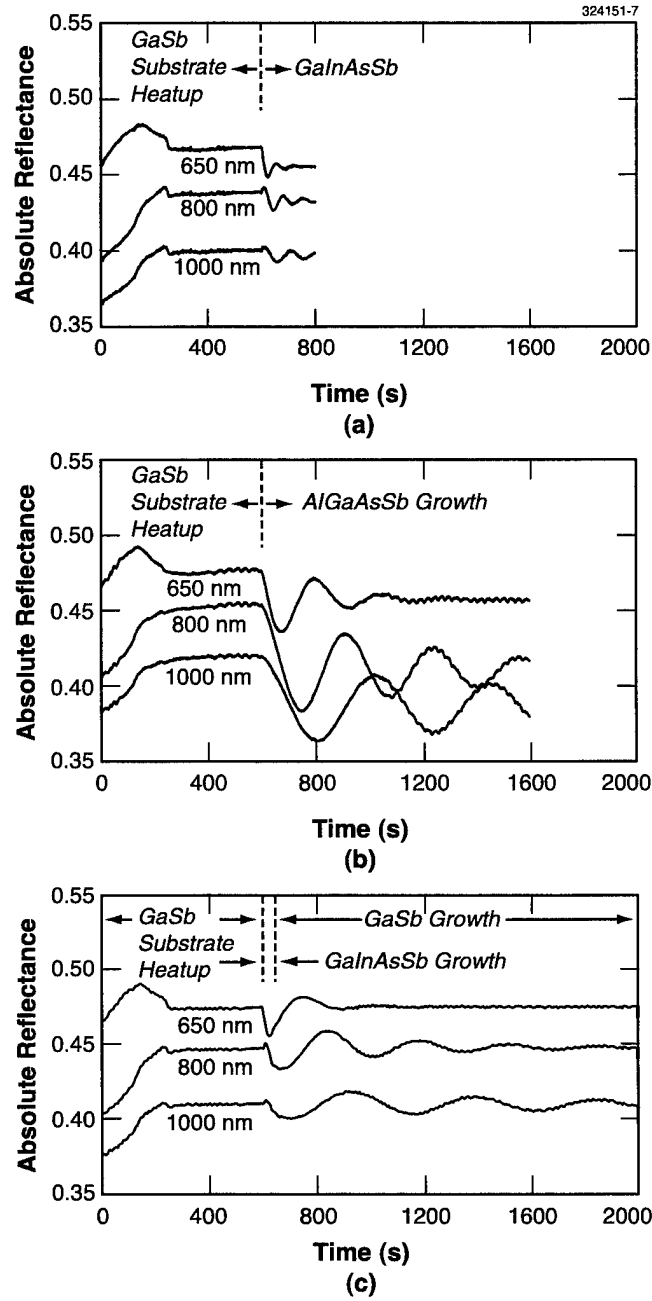
Figure. 2-5. Reflectance as a function of time at 650, 800, and 1000 nm, for the heatup of GaSb substrate (600 s), followed by: (a) growth of lattice-matched GaInAsSb layer at 525°C, (b) growth of lattice-matched AlGaAsSb layer at 550°C, or (c) growth of thin lattice-matched GaInAsSb spacer layer and thick GaSb layer at 525°C. Data are displayed on the same scale to compare the run-to-run heatup similarity.

9

ing heatup is consistent. A deviation from the expected approximately linear increase in reflectance (800- and 1000-nm curves) with temperature is observed between 100 and 250 s. This deviation might be associated with oxide liftoff [9]. The heatup period is followed by 200-s growth of GaInAsSb, shown in Figure 2-5(a), 1000 s of AlGaAsSb growth, shown in Figure 2-5(b), or 42 s of GaInAsSb spacer layer growth and 1500 s of GaSb growth, shown in Figure 2-5(c) (only the initial 1360 s of GaSb layer growth are shown). The GaInAsSb spacer layer is necessary to obtain oscillations from GaSb growth on a GaSb substrate.

Using a VI model [7], the growth rates of GaInAsSb at 525°C, AlGaAsSb at 550°C, and GaSb at 525°C were extracted at several wavelengths between 650 and 1000 nm from the data shown in Figure 2-5. Accurate curve fitting at wavelengths shorter than 750 nm was not possible for the GaInAsSb layer, for two reasons. First, high absorption in the GaInAsSb layer limited the number of Fabry-Perot oscillations, decreasing the accuracy of the least-squares non-linear-regressive curve fitting algorithm. Second, the GaInAsSb alloy composition was such that its complex refractive index N is similar to the GaSb substrate ($N_{GaInAsSb} = 4.73-i*0.73$ vs $N_{GaSb} = 4.97-i*0.65$, at 800 nm and 525°C, based on results from this work), resulting in oscillations with small amplitudes, as seen in Figure 2-5(a). Therefore, this layer had a low signal-to-noise ratio. Wavelengths smaller than 750 nm gave erroneously low growth-rate values. Extracted growth rates from wavelengths between 750 and 1000 nm, however, were consistent to within 0.4%. Therefore, reflectance signals at the longer wavelengths were used for more accurate data analysis. On the other hand, analysis of the AlGaAsSb and GaSb layers indicated that wavelengths as short as 650 nm were still acceptable for extracting growth rates since absorption at these wavelengths is less significant for these materials.

Film thicknesses determined from the in-situ reflectance are 234.0 ± 10.0 nm for the GaInAsSb layer, 273.0 ± 11.0 nm for the AlGaAsSb layer, and 360.0 ± 14.4 nm for the GaSb layer. These values agree well with thicknesses determined ex situ by HRXRD: 231.0 ± 11.6 nm for the GaInAsSb layer, 263.2 ± 13.2 nm for the AlGaAsSb layer, and 369.5 ± 18.5 nm for the GaSb layer. Error in growth-rate determination from the in-situ reflectance is directly related to the ability of the reflectance setup to accurately measure absolute reflectance values. Knowledge of the absolute reflectance, and not simply the relative reflectance, is necessary for the VI model to correctly separate the real part of the refractive index n from the growth rate G yielding physical growth rates instead of optical-thickness growth rates ($n*G$) [7].

Optical constants (n and k) at the growth temperature for all three layers were also extracted using the VI model and are shown in Figure 2-6 for GaInAsSb at 525°C, AlGaAsSb at 550°C, and GaSb at 550°C. The accuracy of these values is limited by the accuracy of the absolute reflectance values determined by the reflectance setup, which has been determined to be ±4% for our system. Unfortunately, little information is available about the refractive indices of these materials at the elevated growth temperatures. Therefore, comparison of our extracted data to literature values is not possible.

C. J. Vineis   C. A. Wang
D. C. Oakley   D. R. Calawa
J. W. Chludzinski K. F. Jensen*
W. G. Breiland*

*Author not at Lincoln Laboratory

10

324151-8
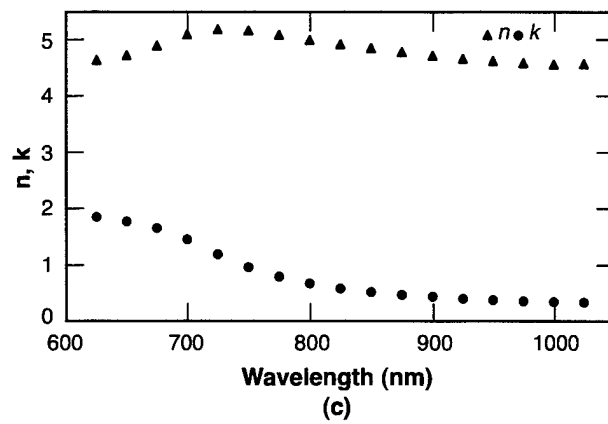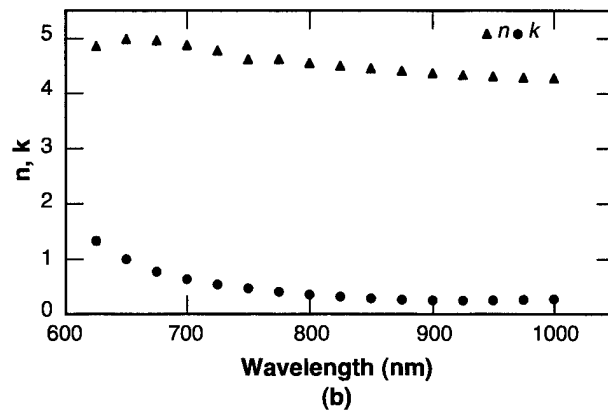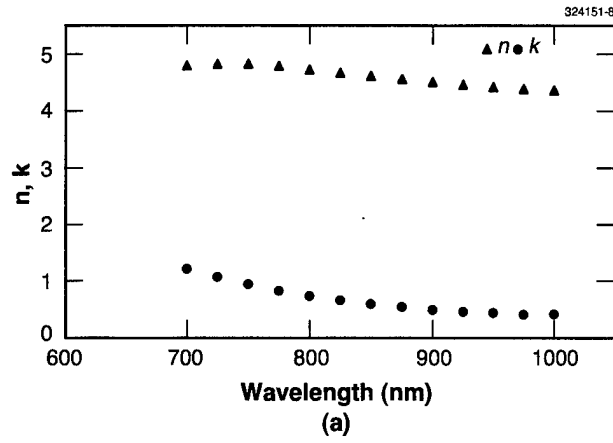
Figure 2-6. Complex refractive indices of (a) GaInAsSb (λ ~ 2.3 µm at 25°C) at 525°C, (b) AlGaAsSb (λ ~ 1.2 µm at 25°C) at 550°C, and (c) GaSb at 550°C. Error of extracted n and k values is ±4%, due to error in accurately determining the absolute reflectance.

11

2.3   EFFECT OF GROWTH TEMPERATURE ON PHOTOLUMINESCENCE OF EPITAXIAL GaInAsSb

GaInAsSb alloys lattice matched to GaSb substrates are of particular interest for thermophotovoltaics (TPVs). Recently, we reported the growth of these alloys by organometallic vapor phase epitaxy (OMVPE) [8], and demonstrated TPV devices with an internal quantum efficiency approaching 90% for devices with a cutoff wavelength of 2.3 μm [10]. Since TPVs are minority carrier devices, high optical quality is desirable. Here, we report the effect of growth temperature on the optical properties of GaInAsSb epilayers which have bandgaps in the wavelength range 2–2.5 μm.

$Ga_{1-x}In_xAs_ySb_{1-y}$ epilayers were grown in a vertical rotating-disk reactor with H_2 carrier gas at a flow rate of 10 slpm and reactor pressure of 150 Torr as described previously [8]. GaInAsSb was grown on (100) Te-doped GaSb substrates with a misorientation of either 2° toward (110) or 6° toward (111)B. Solution trimethylindium, triethylgallium, tertiarybutylarsine, and trimethylantimony were used as organometallic sources. The growth temperature ranged from 525 to 575°C, and the growth rate was typically 2.5 or 5 μm/h. The optical characteristics were evaluated by photoluminescence (PL) which was measured at 4 and 300 K using a PbS detector.

The PL spectra measured at 4 and 300 K are shown in Figure 2-7 for three $Ga_{1-x}In_xAs_ySb_{1-y}$ layers grown at a substrate temperature of 525, 550, or 575°C. Based on the peak emission at 300 K (2160, 2165, and 2156 nm, respectively) and the lattice mismatch, a similar composition of $x \sim 0.12$ and $y \sim 0.1$ was determined. The 4-K PL FWHM increases as the growth temperature increases, and is 4.7, 8.4, and 31.5 meV, respectively. The PL peak emission at 4 K is similar at 1928 and 1925 nm for the layers grown at 525 and 550°C, respectively, but is significantly longer at 2060 nm for the layer grown at 575°C.

The 4- and 300-K PL spectra of $Ga_{1-x}In_xAs_ySb_{1-y}$ epilayers with various composition are shown in Figure 2-8. The layers were grown at 525°C on (100) substrates with a 6° toward (111)B misorientation. The peak emission for the sample shown in Figure 2-8(a) with $x = 0.09, y = 0.08$ is 1818 and 2035 nm at 4 and 300 K, respectively. The 4-K FWHM is 5.3 meV. With increasing x and y values, 4- and 300-K emission increases to 2080 and 2320 nm, respectively, for $x = 0.16, y = 0.15$, shown in Figure 2-8(b); and to 2225 and 2505 nm, respectively, for $x = 0.2, y = 0.18$, shown in Figure 2-8(c). The 4-K FWHM also increases to 7.5 and 25 meV, respectively. Although lattice matched $Ga_{1-x}In_xAs_ySb_{1-y}$ of higher In and As compositions was epitaxially grown, that layer did not exhibit PL at 4 or 300 K. The longest PL emission at 300 K observed in this current study is 2525 nm.

Figure 2-9 summarizes the 4-K PL FWHM data for $Ga_{1-x}In_xAs_ySb_{1-y}$ epilayers which were grown at 525, 550, and 575°C. Several trends are observed. The PL FWHM values are strongly dependent on growth temperature and peak energy (i.e., composition). The lowest PL FWHM values are obtained for layers grown at the lowest temperature of 525°C. The narrowest PL FWHM values are ~5 meV for 4-K peak energy greater than 0.62 eV, and increase sharply below 0.60 eV. On the other hand, the PL FWHM increases below ~0.63 and 0.67 eV for layers grown at 550 and 575°C, respectively. This PL broadening may be related to the thermodynamic stability of the GaInAsSb alloy. A thermodynamic analysis of this

324151-9
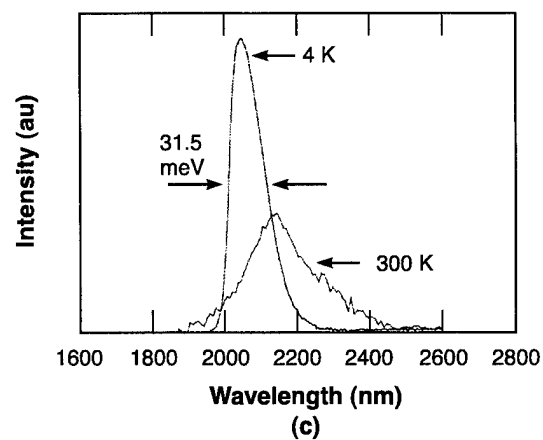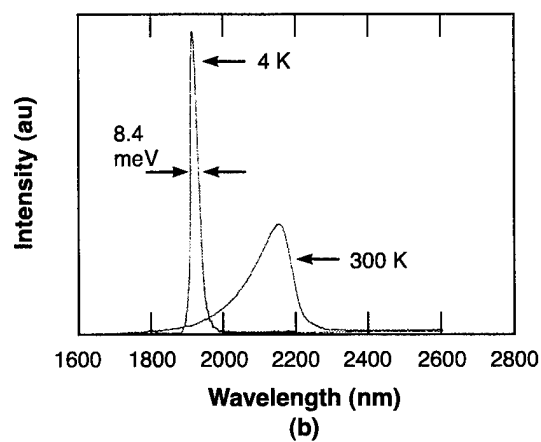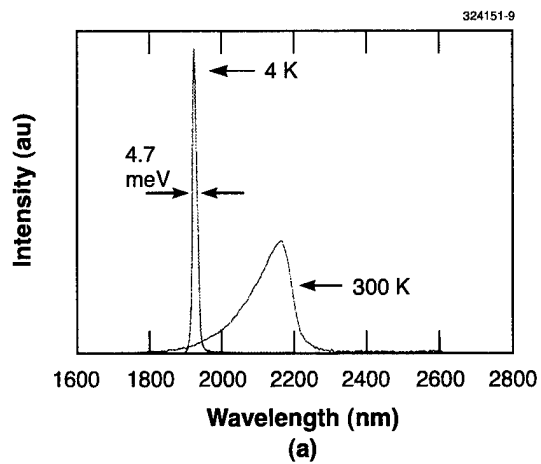
Figure 2-7. Photoluminescence spectra measured at 4 and 300 K of $Ga_{1-x}In_xAs_ySb_{1-y}$ ($x \sim 0.1$, $y \sim 0.1$) grown at (a) 525°C, (b) 550°C, (c) 575°C.

13
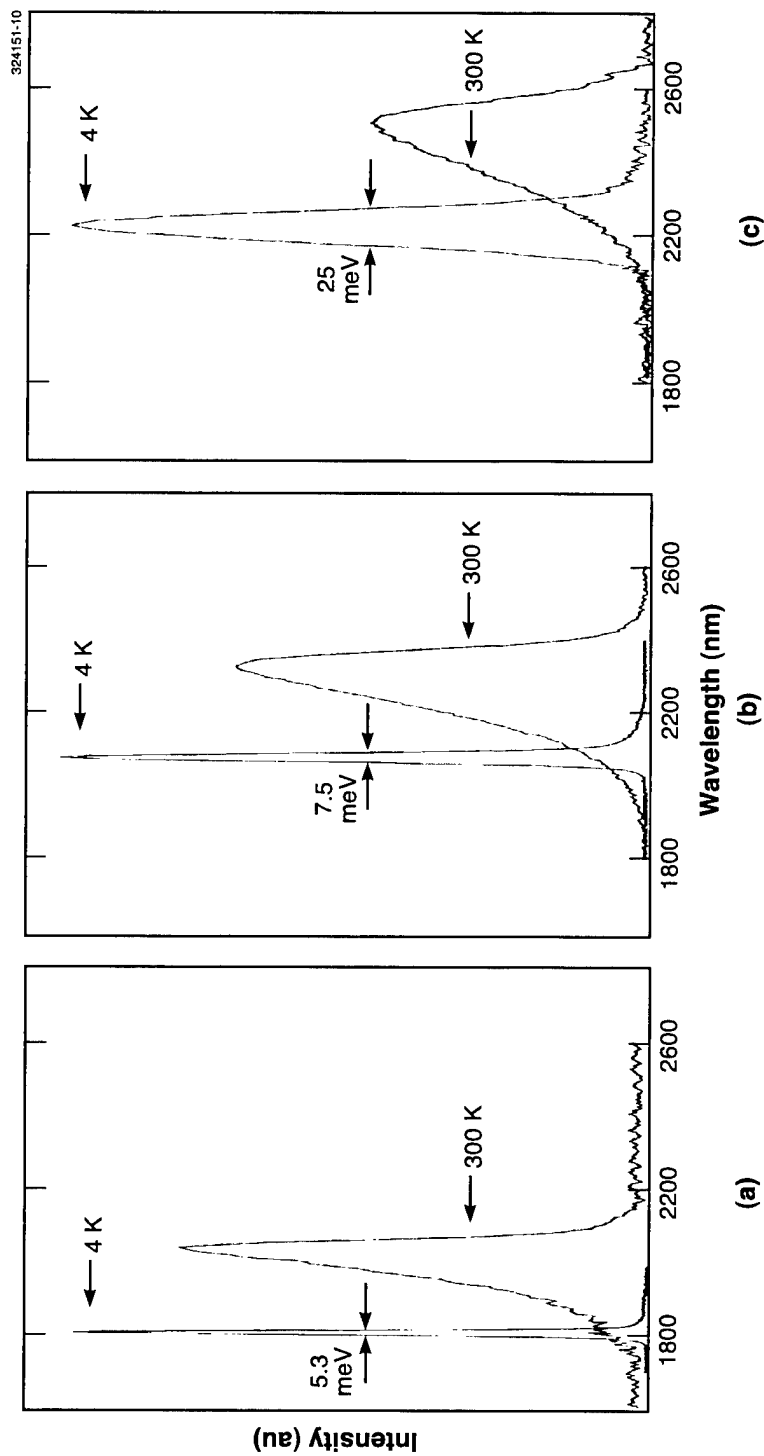
Figure 2-8. Photoluminescence spectra measured at 4 and 300 K of $Ga_{1-x}In_xAs_ySb_{1-y}$ grown at 525°C: (a) x = 0.09, y = 0.08; (b) x = 0.16, y = 0.15; (c) x = 0.20, y = 0.18.

14
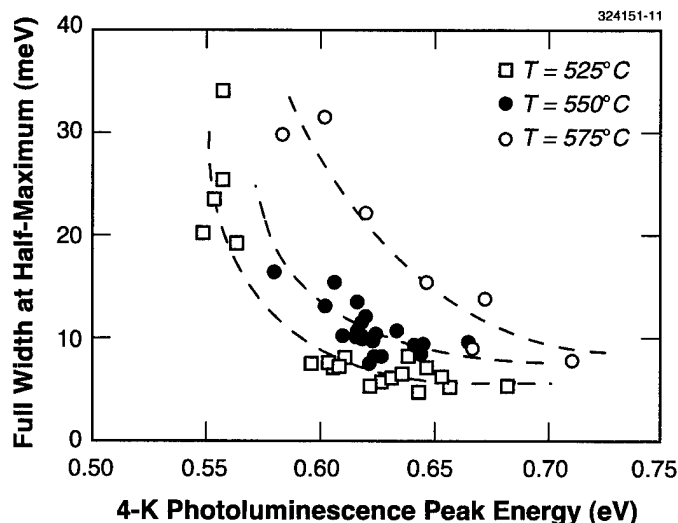
Figure 2-9. Photoluminescence full width at half-maximum measured at 4 K of GaInAsSb layers grown on GaSb substrates at 525 °C (open squares), 550 °C (solid circles), and 575 °C (open circles). Dashed lines provided to guide the eye.

material system predicts a miscibility gap and suggests that these alloys in their bulk state are increasingly unstable with increasing x and y values [11], and can phase separate to GaAs-rich and InSb-rich alloys. Thus, since broadening in PL spectra can be a result of alloy scattering [12], the data are consistent with increased alloy clustering associated with this miscibility gap. The PL results suggest that under nonequilibrium conditions for OMVPE growth, the kinetics can have a significant influence on the extent of penetration into the miscibility gap. Our FWHM values are significantly smaller than those reported previously for OMVPE-grown layers [11],[13],[14], especially for those layers with lower PL peak energy. The smallest FWHM value measured is 4.7 meV at 0.643 eV, which is the lowest value that has been reported for this alloy system grown by OMVPE. Our FWHM values are comparable to those reported for layers grown by molecular beam epitaxy [15] and by liquid phase epitaxy [16].

The energy difference between 4- and 300-K PL peak energy is plotted in Figure 2-10 as a function of the 4-K PL peak energy for epilayers grown at 525, 550, and 575°C. For most of the GaInAsSb alloys grown at 525 or 550°C, this energy difference ranges between 0.05 and 0.07 meV, which is in line with the difference for GaSb [17] and InAs [18] binaries. However, for alloys grown at 575°C, the 4- and 300-K energy difference decreases from about 65 to 10 meV as the 4-K PL peak energy decreases from 0.7 to 0.58 eV. The 4-K PL FWHM values also increased to about 20–30 meV at the lower energy range. These data indicate that estimation of PL emission at room temperature cannot necessarily be extrapolated from low-temperature results and the energy difference based on interpolation from the binaries.

<div align="right">

C. A. Wang   J. W. Chludzinski

D. C. Oakley   D. R. Calawa

</div>

15
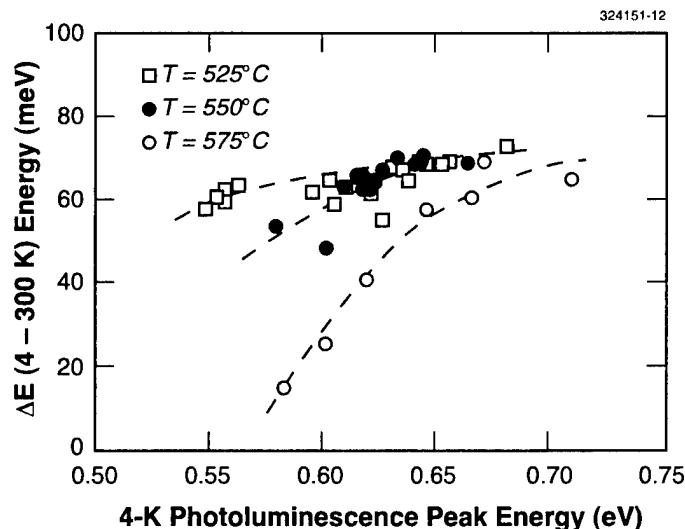
Figure 2-10. Difference between 4- and 300-K photoluminescence peak energy as a function of 4-K peak energy. Layers were grown at 525°C (open squares), 550°C (solid circles), and 575°C (open circles). Dashed lines provided to guide the eye.

REFERENCES

1. J. P. Donnelly, J. N. Walpole, G. E. Betts, S. H. Groves, J. D. Woodhouse, F. J. O'Donnell, L. J. Missaggia, R. J. Bailey, and A. Napoleone, *IEEE Photon. Technol. Lett.* **8**, 1450 (1996).

2. G. E. Betts, J. P. Donnelly, J. N. Walpole, S. H. Groves, F. J. O'Donnell, L. J. Missaggia, R. J. Bailey, and A. Napoleone, *IEEE Trans. Microwave Theory Tech.* **45**, 1280 (1997).

3. J. C. Livas, S. R. Chinn, E. S. Kintzer, J. N. Walpole, C. A. Wang, and L. J. Missaggia, *Proc. SPIE* **2148**, 107 (1995).

4. D. Zhou, P. R. Prucnal, and I. Glesk, *IEEE Photon. Technol. Lett.* **10**, 781 (1998).

5. I. P. Herman, *Optical Diagnostics for Thin Film Processing* (Academic, New York, 1996).

6. H. Sankur, W. Southwell, and R. Hall, *J. Electron. Mater.* **20**, 1099 (1991).

7. W. G. Breiland and K. P. Killeen, *J. Appl. Phys.* **78**, 6726 (1995).

8. C. A. Wang, *J. Cryst. Growth* **191**, 631 (1998).

9. N. J. Mason and P. J. Walker, Proceedings of ICMOVPE IX, La Jolla, Calif., 1998.

10. H. K. Choi, C. A. Wang, G. W. Turner, M. J. Manfra, D. L. Spears, G. W. Charache, L. R. Danielson, and D. M. Depoy, *Appl. Phys. Lett.* **71**, 3758 (1997).

16

11. M. J. Cherng, H. R. Jen, C. A. Larsen, G. B. Stringfellow, H. Lundt, and P. C. Taylor, *J. Cryst. Growth* **77**, 408 (1986).

12. J. Singh and K. K. Bajaj, *Appl. Phys. Lett.* **44**, 1075 (1984).

13. J. Shin, T. C. Hsu, Y. Hsu, and G. B. Stringfellow, *J. Cryst. Growth* **179**, 1 (1997).

14. M. Sopanen, T. Koljonen, H. Lipsanen, and T. Tuomi, *J. Cryst. Growth* **145**, 492 (1994).

15. C. A. Wang, H. K. Choi, G. W. Turner, D. L. Spears, M. J. Manfra, and G. W. Charache, *3rd NREL Conference on the Thermophotovoltaic Generation of Electricity*, Vol. 401 of *AIP Conference Proceedings* (American Institute of Physics, Woodbury, N.Y., 1997), p. 75.

16. E. Tournie, J.-L. Lazzari, F. Pitard, C. Alibert, A. Joullie, and B. Lambert, *J. Appl. Phys.* **68**, 5936 (1990).

17. S. C. Chen and Y. K. Su, *J. Appl. Phys.* **66**, 350 (1989).

18. Z. M. Fang, K. Y. Ma, D. H. Jaw, R. M. Cohen, and G. B. Stringfellow, *J. Appl. Phys.* **67**, 7034 (1990).

3. SUBMICROMETER TECHNOLOGY

3.1 OUTGASSING OF 193-nm RESISTS

The initial research that led to the development of 193-nm-wavelength photolithography was sponsored by DARPA. As this technology approaches commercial acceptance, there is increasing interest by the potential users in detailed investigation of operational issues. This report summarizes a study of some of the fundamental mechanisms that affect optics contamination and thereby impact tool lifetime. This work was funded under a cooperative research and development agreement (CRDA) with SEMATECH.

Lens contamination, caused by resist outgassing, is a serious concern in photolithography systems because the photoresist-covered surface, which is chemically active, is held in close proximity to the final lens element. A large body of anecdotal evidence exists that shows 193-nm laser radiation can interact with trace levels of organic vapors to contaminate optical surfaces. The 6.4-eV photon energy is high enough to activate organic photochemical reactions, and irradiation of air at 193 nm generates ozone (and other metastable oxygen-containing radicals), opening up additional pathways for activating both gas-gas and gas-surface reactions which may be deleterious.

We have performed a three-part study aimed at assessing the relationship between resist outgassing and potential lens contamination at 193 nm. First, we have performed quantitative measurements of outgassing flux and product distribution from prototype 193-nm resists using both a gas chromatograph–mass spectrometer (GCMS) and a quartz microbalance. Then, based on these findings, we have performed experimental studies with the GCMS on atmospheric and surface reactions that occur with the most common outgassed products. These include unimolecular photochemical reactions, bimolecular reactions with ozone, and determination of gas-surface equilibria. Finally, we have performed low-fluence (<0.5 mJ/cm^2 per pulse) laser chemical vapor deposition experiments on SiO$_2$ and CaF$_2$ surfaces using vapors identified in the first experiment at partial pressures in the 1–10-ppm range and have recorded and compared deposition efficiencies. The deposits were usually quite thin (<5 nm) for our limited exposures ($\sim$1 million pulses) and we used ultraviolet–vacuum ultraviolet spectrophotometry, interferometric calorimetry, and angle-resolved x-ray photoelectron spectroscopy to inspect and quantify the deposits.

There were two categories of experiments performed: those aimed specifically at measuring outgassing from resists and those aimed at determining the fate of outgassed products vis-à-vis subsequent reactions in the atmosphere or on nearby surfaces. All the experiments used the apparatus shown in Figure 3-1, which consisted of a single, wavelength-selectable laser source whose beam could be directed to one of two locations. The first was a quartz-crystal microbalance (QCM) operating at a resonant frequency of approximately 6 MHz, and the second was a stainless steel chamber alternately exhausted into a two-stage cryotrap in series with a GCMS, a flame ionization detector, and/or an ozone monitor. This combined apparatus was used for quantitative determination of resist outgassing fluxes and composition, and was also equipped to deliver calibrated gas mixtures simulating contaminated environments. In addition, we used vacuum-ultraviolet spectrophotometry and interferometric calorimetry to inspect optical surfaces that had been intentionally contaminated.
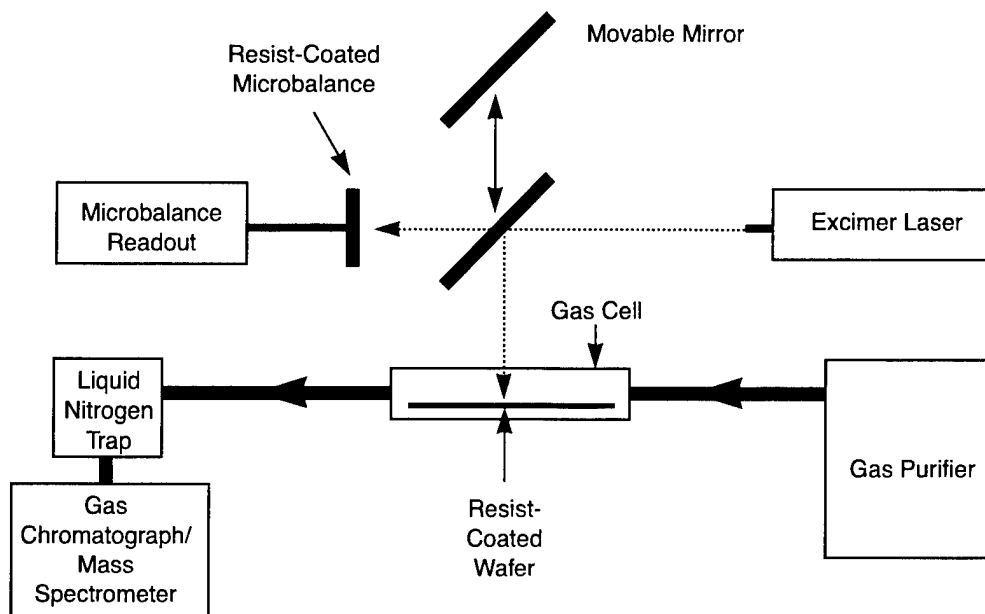
Figure 3-1. Experimental apparatus used to quantify photoresist outgassing rates. The setup includes a quartz crystal microbalance (QCM) and a gas chromatograph–mass spectrometer (GCMS).

The QCM is well suited to measuring the outgassing flux as a function of time, but does not identify the chemical species. The instrument records the net mass change of the sample with a temporal resolution of 1 s. Figure 3-2 illustrates typical datasets obtained for two different types of resist, one with a high activation energy and the other with a low activation energy. Both samples show an initial increase in film thickness due to photooxidation of the material, and this effect can mask any instantaneous mass evolution during exposure. Notice that the low activation energy material displays a continuing loss of film thickness, indicative of outgassing, for several minutes after the exposure. This is a significant observation because it implies that, although the photolithography system will expose the resist in a series of small fields, the entire wafer will be outgassing at the end of the exposure, which will increase the total flux seen by the optical elements in the system.

The GCMS data complements the QCM data. It is used to determine the chemical identity of the out-gassed species, but it requires long sampling integration times to achieve the needed sensitivity and therefore does not provide any temporal information about the product evolution. The GCMS records the time-integrated total product evolution with a time resolution of ~2 min. Figure 3-3 shows a representative chromatograph for an acrylic resist. In this test the resist-coated substrate was irradiated for a total dose of 8 mJ/cm^2 at a fluence of 0.1 mJ/cm^2 per pulse, and the exposure was accomplished in less than 1 s. The
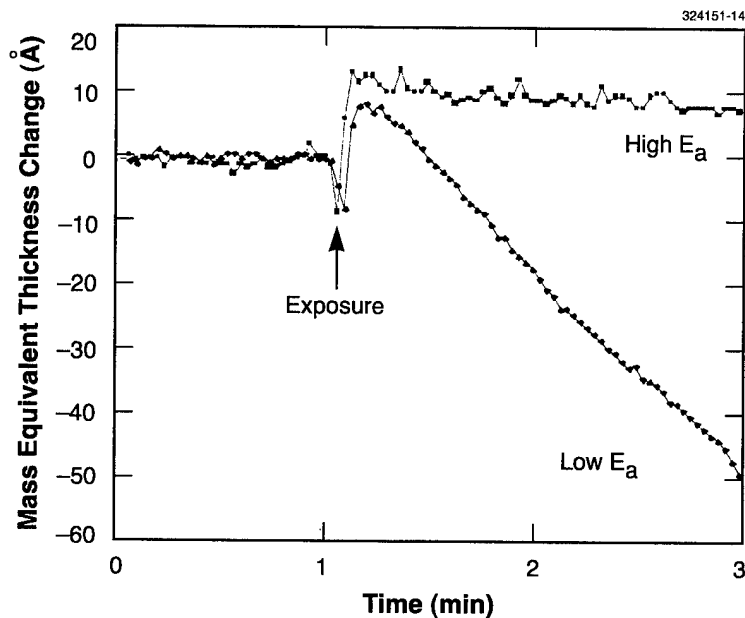
Figure 3-2. Film thickness variation as function of time for two different resists after exposure to 193-nm irradiation. The net change in mass is measured using a QCM, and this is used to compute an equivalent change in film thickness. E_a = activation energy.

known chemical components of the resist include: methyl methacrylate, methacrylic acid, t-butyl methacrylate, isobornyl methacrylate, and di-t-butylphenyl iodonium trifluoromethane sulfonate. The outgassed species are summarized in Table 3-1 and include components attributed to the dissolution-inhibiting protecting group, photoacid generator, residual solvents, and the polymer itself. Other resists have been tested and each reveals a unique chemical outgassing signature.

Both the QCM and GCMS data indicate outgassing fluxes in the range 10^{11}–10^{14} molecules/cm^2 s for the first 2 min after laser exposure. Based on these data the partial pressures of the organic vapors can be calculated, provided that the geometry and gas flow rates around the exposed wafer are known. In general, the contamination levels will probably be in the mid-ppb range for most resists.

The goal of these experiments is to develop a quantitative basis for comparing the effects of different resists on lens contamination. Since the reactions are surface mediated, we need only consider laser-surface reactions, and hence the adsorption behavior of the contaminants on the lens surfaces becomes important. To better understand this behavior, we can use the outgassing data to estimate localized partial pressures of contamination, then calculate the surface coverage of these compounds on the lenses by using the Braunauer-Emmet-Teller (BET) adsorption isotherm. The BET adsorption isotherms for three common contaminants are shown in Figure 3-4, where it becomes clear that high boiling point compounds exhibit

324151-15

$\left[\begin{array}{c} \\ \end{array}\right] I^+ X^- \longrightarrow H^+X^- +$ Organic Fragments

Toluene

Isobutene

t-Butyl benzene

Iodo-t-butyl benzene

Acetone   Benzene   Camphene

Solvent Hydrolysis Products

Isobutene dimer

0 2 4 6 8 10 12 14 16 18 20 22 24 26 28 30

Time (min)
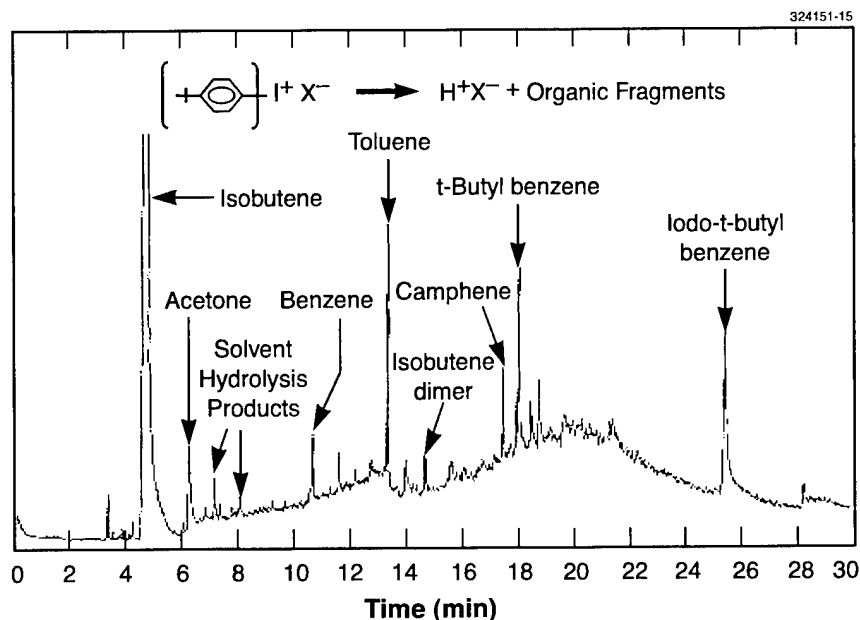
Figure 3-3. Chemical analysis of outgassed species. The GCMS was used to identify the chemical components released after an acrylic photoresist was exposed to 193-nm radiation.

the highest surface coverages. Once the surface coverages are known, the probability for a chemical to cause a contamination event can be estimated as the product of the surface coverage times its absorption cross section at 193 nm. The product of these two parameters is plotted vs partial pressure for the same three contaminants in Figure 3-5. From this, it becomes clear that factors other than simple outgassing flux must be considered when redesigning a photoresist for reduced contamination risk. For example, a typical resist that outgasses 99% isobutene and 1% iodobenzene will exhibit a contamination rate from the iodobenzene that is ~100 000 × higher than that from the isobutene. This stems from their vastly different condensation and 193-nm absorption behaviors. This information has been passed to the U.S. photoresist suppliers, and new resist formulations have been engineered and are under evaluation by the U.S. chip makers.

R. R. Kunz
D. K. Downs

TABLE 3-1
Summary of Outgassed Species

Compound	Source	Fraction
Isobutene	t-Butyl ester hydrolysis	65.84
Methanol	Mechanism not clear	27.16
Acetaldehyde	Mechanism not clear	1.93
Acetone	Mechanism not clear	1.89
t-Butyl benzene	Photoacid generator	0.95
Toluene	Photoacid generator	0.78
1-Iodo-4-t-butyl benzene	Photoacid generator	0.45
Camphene	Isobornyl ester hydrolysis	0.41
3-Methoxy-1-propene	Solvent hydrolysis	0.15
Benzene	Photoacid generator	0.13
Ethanol	Mechanism not clear	0.08
1-Methoxy-2-propene	Solvent hydrolysis	0.03
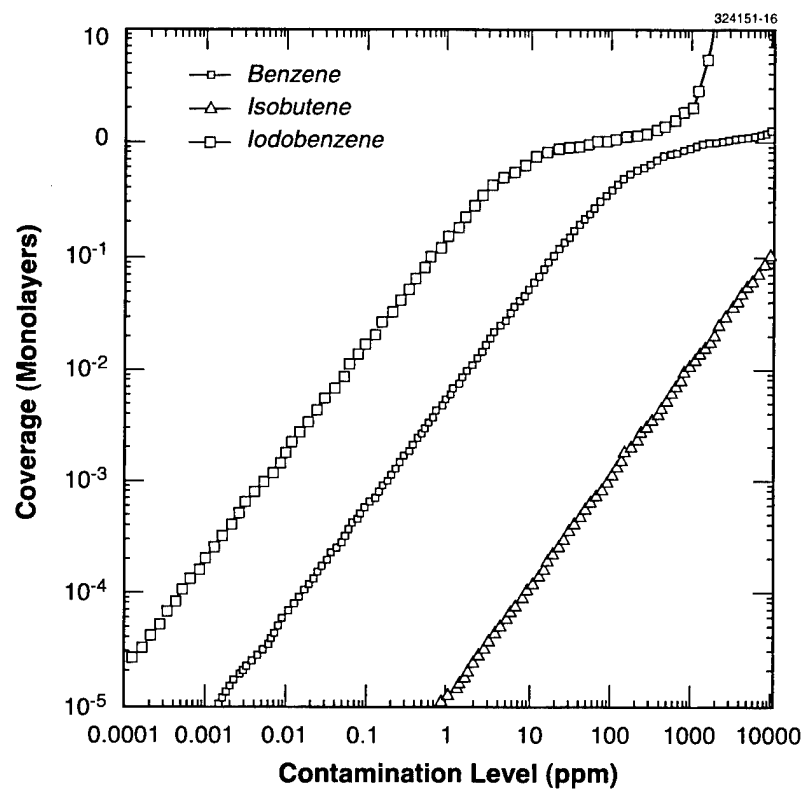
Figure 3-4. Calculation of equilibrium surface coverage of adsorbed layers of three chemical species as function of ambient concentration levels.

324151-17
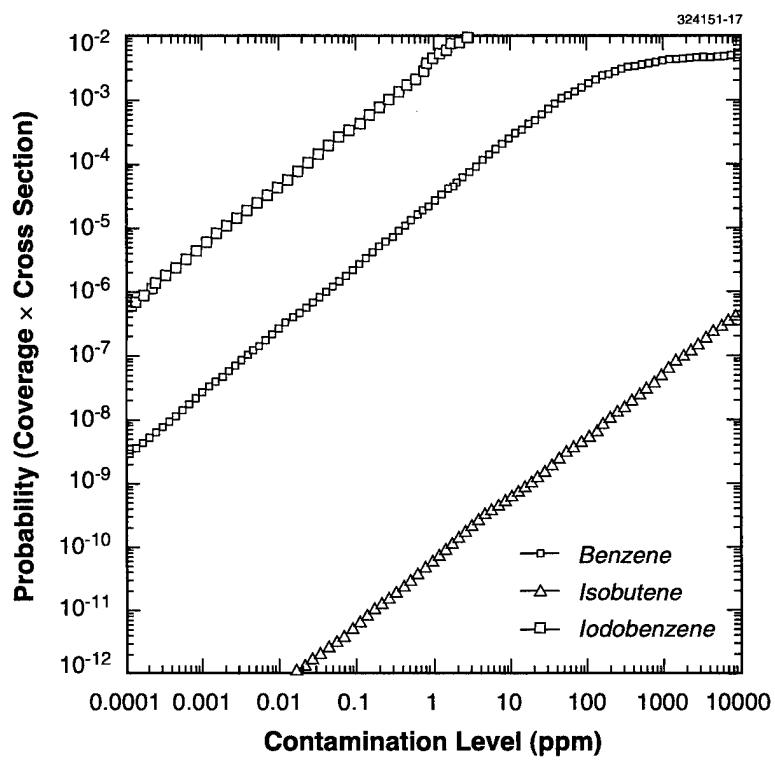
Figure 3-5. Calculation of photoabsorption probability as function of ambient concentration.

4. BIOSENSOR AND MOLECULAR TECHNOLOGIES

4.1 NOVEL BIOELECTRONIC SENSOR FOR RAPID, SENSITIVE IDENTIFICATION OF PATHOGENS

A new bioelectronic sensor is being developed which can identify pathogenic bacteria and viruses and would thus be useful for biological agent detection, medical diagnostics, and other applications. White blood cells, which function within the human body to detect pathogens, respond in a fashion which is much more rapid, sensitive, and specific than currently available man-made sensors. Therefore, our approach is to directly integrate live white blood cells with microelectronics. Here, we will briefly explain the sensor design and present experimental results which demonstrate the feasibility of this approach.

Because this project uses a biological system to warn of hazardous substances in the environment, it is called CANARY (Cellular Analysis and Notification of Antigen Risks and Yields). As shown in Figure 4-1, CANARY utilizes a type of white blood cell known as a B lymphocyte which is covered with antibodies. Different B cells can have antibodies which specifically bind to the antigens (surface features) of different pathogens. For this sensor the B cells are genetically engineered to produce aequorin, a bioluminescent protein originally found in a glowing species of jellyfish, and the cells are attached to the surface of a charge-coupled device (CCD) imaging array. Figure 4-1 illustrates how this system would work: (1) Suspected bioagents or other potential pathogens can be injected into the cell culture liquid which surrounds the B cells. (2) The B cells have antibodies which are specific for certain bioagents. If one of those bioagents is present in the sample, it will bind to the antibodies on the surface of an appropriate B cell. (3) Binding of a bioagent to a B cell's antibodies triggers a cascade of biochemical events inside the cell. This cascade serves to greatly amplify the signal, and it results in the release of calcium ions inside the cell. (4) In the presence of calcium, the genetically added aequorin protein emits photons. Thus, B cells which detect bioagents will begin to glow. (5) Light from glowing B cells is detected by the CCD imager underneath the cells. Cells specific for different pathogens can be attached to different regions of the CCD, so the location of the glowing cells indicates what sort of virus or bacterium has been detected.

To demonstrate the validity of this approach, we have created suitable genetically engineered B cells. We obtained mouse B cells which have antibodies that are specific for phosphorylcholine-ovalbumin [1], a molecule which is illustrated schematically in Figure 4-2. Because these cells are immortal, they can be grown for periods of several years in an artificial environment with the appropriate temperature, gases, and culture medium. We obtained the jellyfish aequorin gene [2] and permanently inserted it into the genome of the B cells.

The resulting cells exhibited a high degree of specificity in our experiments. As shown in Figure 4-2, when the cells were exposed to phosphorylcholine-ovalbumin, their photon emission rate increased by a factor of 130 in approximately 30 s. In contrast, when the cells were exposed to just phosphorylcholine or just ovalbumin, there was very little response. Likewise, the cells gave no response to bovine serum

27

324151-18

(1)
Inject Possible Bioagents into
Cell Culture Liquid

(2)
B Cell Antibodies Recognize
Bioagent Antigens

Antibodies

B Cell
with Added
Aequorin
Gene

(3) Biochemical
Signal
Amplification
Releases Ca^{2+}

(4) Ca^{2+} Makes
Aequorin Emit
Photons

Transparent Substrate

CCD Imaging Array | (5) Detect Glowing Cells
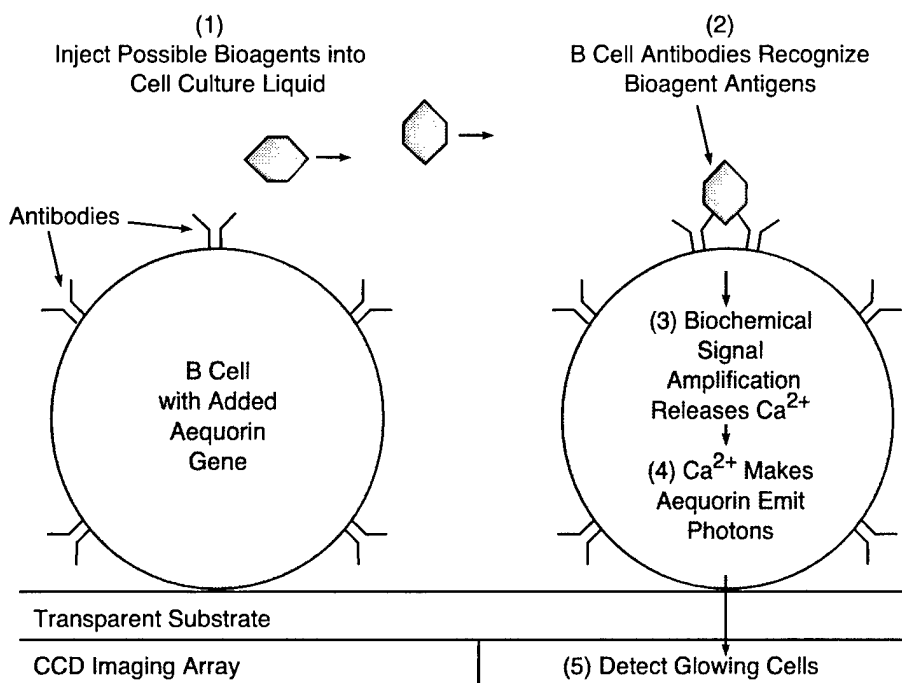
Figure 4-1. Fundamental principles of CANARY bioelectronic sensor.

324151-19

3.5×10^5

— PC-Ovalbumin
--- PC
— — Ovalbumin
..... Other

Stimulant
Injected

Photons/Second

3.0
2.5
2.0
1.5
1.0
0.5
0

-50   0   50   100   150   200
Time (s)
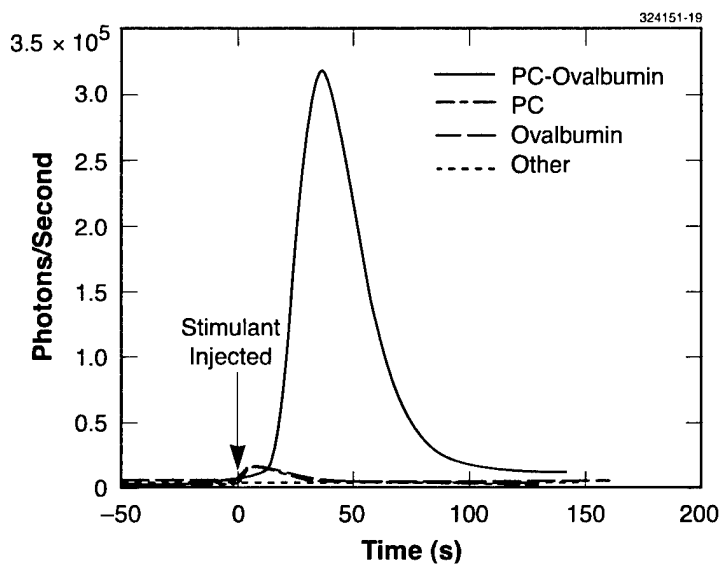
Figure 4-2. Specificity of luminescent B-cell response. The peak/background value is 130 for phosphorylcholine (PC)-ovalbumin, compared with ~4 for PC or ovalbumin alone and 1 for other substances (B. subtilis, E. coli, yeast, phage M13, and sand).

28

324151-20P

Elastomeric Cover

Bioagent
Injection

CCD Imager

Nutrient
Media

Glass
Substrate
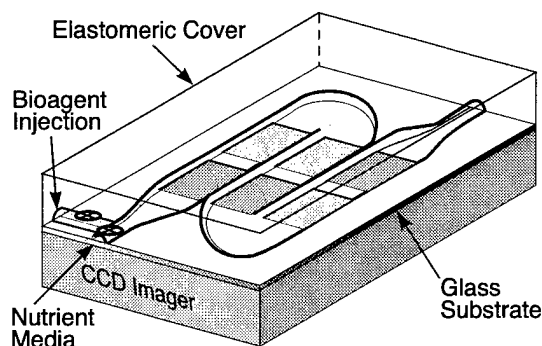
(a)
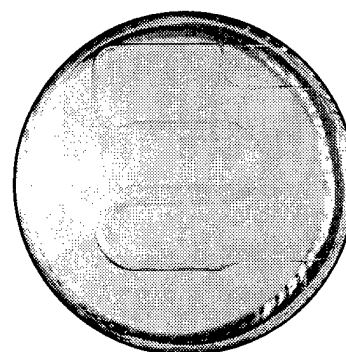
Serpentine Channel Widths = 1 to 3 mm

(b)
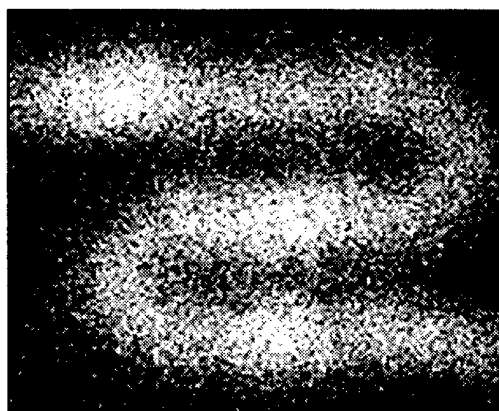
(c)

Figure 4-3. Microfluidics and charge-coupled device (CCD) hardware for CANARY sensor: (a) Concept, (b) fabricated chip with microfluidic channel, (c) CCD image of stimulated B cells in chip.

albumin, which is similar to ovalbumin. In addition, the cells did not respond to common contaminants which might be present in environmental samples, such as a typical Gram-positive bacterium (*B. subtilis*), a typical Gram-negative bacterium (*E. coli*), yeast (a stand-in for fungal spores), a virus (phage M13), and sand. Therefore, the B cells' responses make them highly suitable for use in a sensor. When they are exposed to the substance they were designed to detect, they respond in a very rapid and sensitive fashion. When they are exposed to other substances, they have virtually no response.

Prototype hardware has also been developed for the sensor. As depicted in Figure 4-3(a), the sensor requires microfluidics and a CCD imager. B cells specific for different pathogens could be attached in different sectors within a serpentine microfluidic channel. The microfluidic system enables nutrients and

potential bioagents to be carried to the B cells, and it also permits the removal of waste from the cell chambers. Figure 4-3(b) shows a recently fabricated microfluidic chip. For preliminary tests, the microfluidic chip was loaded with B cells, which were all stimulated to glow simultaneously. The result is shown in Figure 4-3(c).

Now that the fundamental feasibility of this approach has been demonstrated, continuing work will focus more on optimizing the fieldability of the sensor. By creating standardized B cells and antibody gene constructs, we are developing a practical technique for rapidly producing cells which are specific for new bioagents. Moreover, in order to produce cells which have improved robustness, lifetime, and attachment characteristics, we are both refining the properties of the B cells and also genetically adding antibodies to other cell types. Finally, we are preparing new microfluidic and imaging hardware for future tests of the sensor.

T. H. Rider   M. S. Petrovick
A. M. Young   L. T. Smith
M. A. Hollis   J. Chen

REFERENCES

1.   V. S. Parikh, G. A. Bishop, K. J. Liu, B. T. Do, M. R. Ghosh, B. S. Kim, and P. W. Tucker, *J. Exp. Med.* **176**, 1025 (1992).

2.   D. Button and M. Brownstein, *Cell Calcium* **14**, 663 (1993).

5. MICROELECTRONICS

5.1 DEFORMATION OF Si MEMBRANES TO SPHERICAL SURFACES

Very significant performance benefits could be achieved if focal planes with spherical or cylindrical focal surfaces could be fabricated. Simple, high-performance optical devices tend to produce curved image surfaces, and optical designers must add optical elements (decreasing performance and adding weight, cost, and complexity) to produce flat image planes. Use of a curved focal surface would ameliorate this problem, since the focal surfaces for many simple optical systems are often spherical sections. Calculations for prototype micro-air vehicles indicate that significant improvements in the modulation transfer function will be obtained if a spherical focal surface is used instead of a planar one.

Lincoln Laboratory has had considerable experience fabricating back surface illuminated Si charge-coupled device (CCD) imaging arrays. During this process, imager wafers are thinned to membranes between 12 and 50 μm thick. These thin membranes, supported by a thick rim around the perimeter of the wafer, have remarkable strength, presenting the possibility of elastically deforming low-noise large-area imager arrays so they may be curved permanently to nonplanar substrates.

Preliminary studies of the deformation of thinned Si disks indicate mechanical failure occurs when the disk covers a few tenths of a steradian. To increase the solid angle that a curved focal plane could cover, blank Si petal membranes, with a geometry similar to a Maltese cross, have been fabricated. The individual arms, or petals, of this arrangement will be designed to mesh together as the device is deformed to a spherical surface. A blank Si wafer was thinned to 20 μm and patterned with the petal design, separating it from the rim-thinned wafer. As shown in Figure 5-1, there are 16 petals joined at the center. The slits between
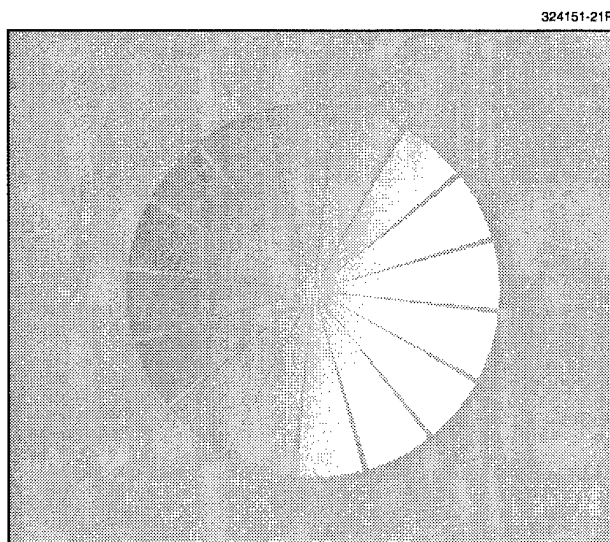
Figure 5-1. Blank silicon membrane thinned to 20 μm and patterned to form a 16-petal structure.
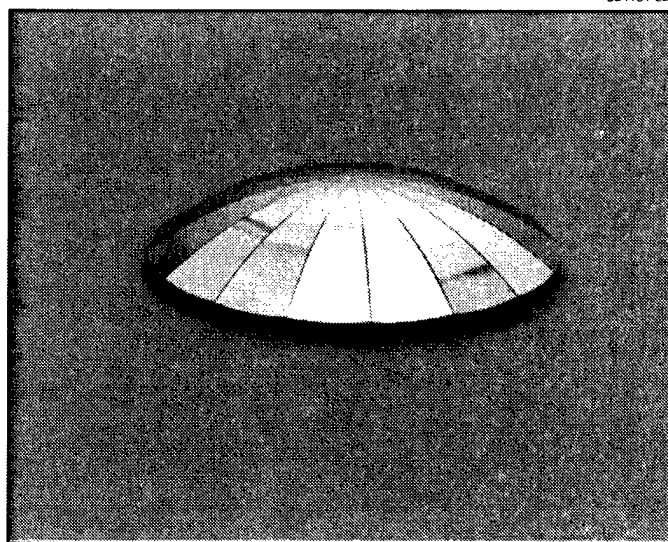
Figure 5-2. Patterned Si membrane deformed about a 39-mm radius of curvature. The solid angle covered by the Si exceeds 1.3 steradians.

the petals have the appropriate curvature so they will mesh as the petal is deformed around a given spherical section. In Figure 5-2, the petal membrane has been deformed to a spherical section with a radius of 39 mm, covering 1.3 steradians. Gaps are still present between the petals, but it is believed a change in loading conditions will help narrow these seams to dimensions on the order of a pixel in a CCD, around 20 μm. This work suggests a petal CCD chip, with pixels arranged along polar coordinates, could be fabricated and take advantage of the improvements accompanying the use of curved focal surfaces.

J. A. Gregory
A. H. Loomis

32

6. ANALOG DEVICE TECHNOLOGY

6.1 MEASUREMENT OF THE ENERGY SENSITIVITY OF A SUPERCONDUCTIVE COMPARATOR

Superconductive high-speed comparators, such as the quantum flux parametron (QFP) [1], are critical elements in the front ends of high-resolution analog-to-digital (A/D) converters [2]–[4], timing discriminators, and other analog circuits. One important figure of merit for a comparator is its energy sensitivity S_ε. S_ε is the product of the minimum energy that can be detected during a measurement time, Δt, and Δt. The comparator is more sensitive the smaller S_ε is. Planck's constant h (6×10^{-34} J s) is a lower bound on S_ε because Heisenberg's uncertainty principle may not be violated. Here, we describe an experimental procedure to measure the energy sensitivity of a superconductive comparator and to compare it with the theoretical sensitivity of an ideal comparator.

Figure 6-1(a) shows the schematic of a QFP comparator ([1] gives more detailed operation of the QFP and readout). A small signal I_{INPUT} is applied to the input of the comparator. An activation or "exciter" current $I_{EXCITER}$ is applied to cause the QFP to generate a large downward current in the inductor L_{READ} if I_{INPUT} is positive and a large upward current in L_{READ} if I_{INPUT} is negative; the timing of input signals is shown in Figure 6-1(b). The direction of the current in L_{READ} is read out by applying a bias current I_{BIAS} to the superconducting quantum interference device (SQUID) containing the elements L_{READ}-J_3-J_4. If the current in L_{READ} is positive, then the SQUID enters the voltage state, and a positive voltage (a Josephson junction gap voltage) is generated at the node $V_{MONITOR}$. If the current in L_{READ} is negative, no voltage is produced at the node $V_{MONITOR}$. This voltage can be read out as a digital "1" or "0" and recorded by semiconductor electronics.

Previous work on superconductive comparators has centered around the measurement of the "gray" zone using the type of experiment illustrated in Figure 6-2. The input is fixed at a dc current level while the comparator is repeatedly clocked. The digital output state of the comparator is detected by room-temperature electronics. If the dc input has a value such that the comparator operates at its balance point, then thermal noise in the comparator will cause it to generate a random output (0 or 1) due to thermal noise fluctuations. The fraction of clock cycles in which the comparator generates a 1 is recorded as a probability. The experiment is repeated for a range of dc input currents, and the results are plotted. Figure 6-3 shows a typical experimental plot of the gray zone, in this case for a QFP comparator. The width of the gray zone is determined by the intrinsic thermal noise in the comparator and by the comparator's dynamics. Investigators have studied the shape of the gray zone with respect to circuit parameter values, temperature, and shape of the comparator excitation pulse, and there has been good agreement between measurements and theory [5]–[7].

From the slope of the gray zone and by assuming that the digital 1s and 0s are uncorrelated, the energy sensitivity can be calculated by the theory in [7]. However, the assumption that the data are uncorrelated (spectrally white) must be demonstrated. Furthermore, the energy sensitivity should be directly

33

324151-24
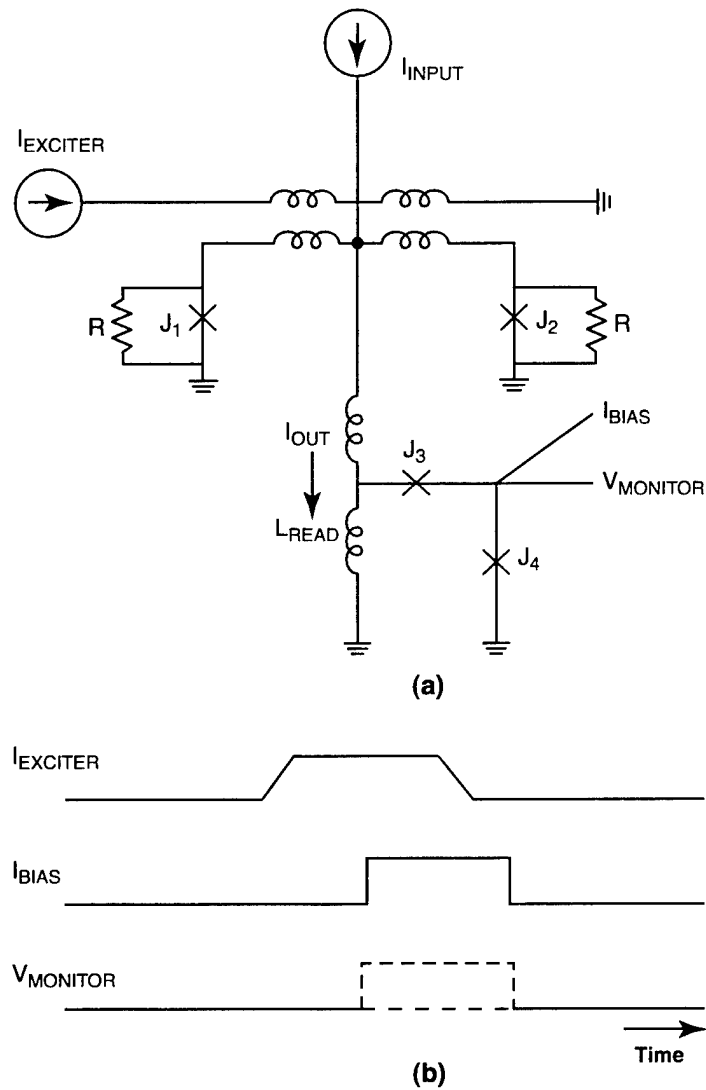
Figure 6-1. (a) Schematic of the quantum flux parametron (QFP) comparator with superconductive quantum interference device (SQUID) readout circuit. (b) Timing of inputs and outputs.

34

Clock

Comparator
(at 4.2 K)

Sig In   Out   Amp   Low-Pass
Filter

Probability (I_{DC})

I_{DC}

V_{OUT}

0
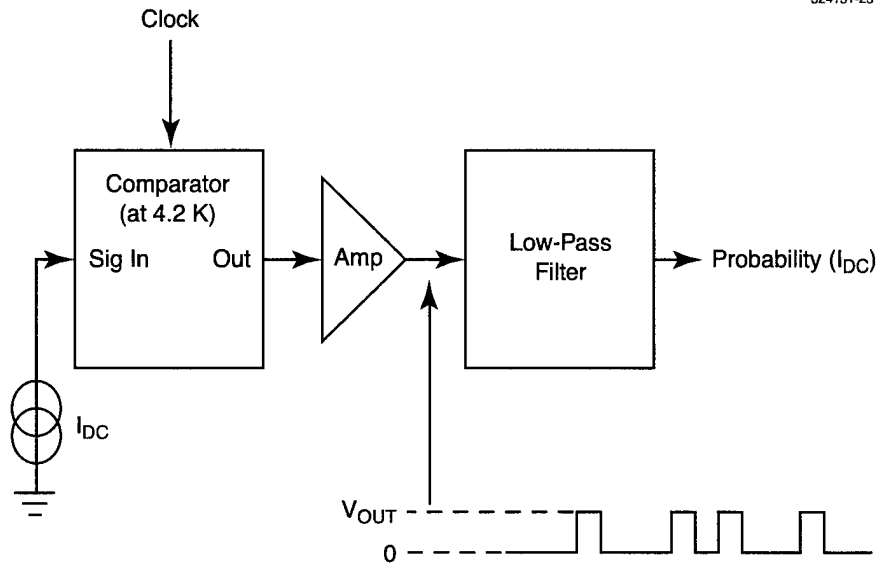
*Figure 6-2. Experimental setup to measure gray zone of comparator. A dc input is applied to the input of a supercon-
ductive comparator under test. The data (1s and 0s) are amplified and read out to room temperature where they are
low-pass filtered. The output voltage can be converted to a probability that the output is a 1.*

1.0

0.5

0

Probability (Output = "1")

Input Offset
= −1.22 µA

−5   −4   −3   −2   −1   0   1   2   3

Input Current (µA)
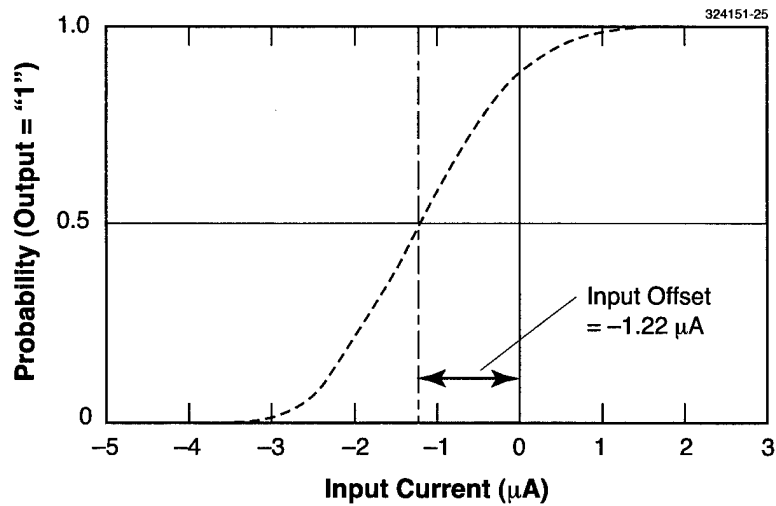
Figure 6-3. Measurement of gray zone of QFP.
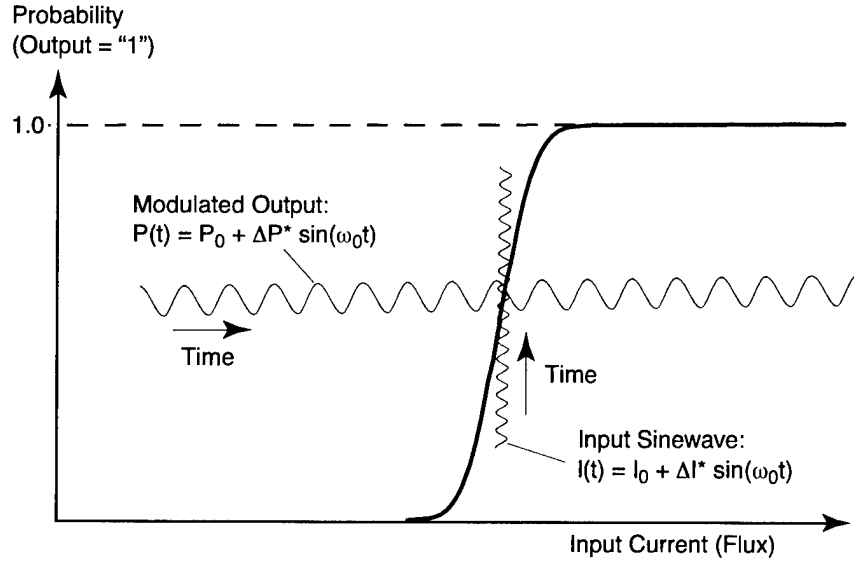
Figure 6-4. Small sinewave added to the dc bias at the input of the comparator. Output probability is sinusoidally modulated.

measured and compared to the value calculated based on the slope of the gray zone. We have designed an experiment to achieve these objectives. Suppose that we perform the experiment shown in Figure 6-2, but this time we add a small ac waveform to the dc bias, as shown in Figure 6-4. The input sinewave modulates the probability that the output will generate a 1 as follows:

$$P_{OUT}(t) = P_0 + \Delta P \sin(\omega_0 t) \tag{6.1}$$

If we assume that the output of the comparator is a sequence of impulses, each of which has a probability $P_{OUT}(t)$ of being a 1, then we can write an expression for the autocorrelation function of this modulated pulse train. The power spectral density $S(\omega)$, which is the Fourier transform of this autocorrelation function, is given by

$$S(\omega) = 2f_B\left[P_0(1-P_0) - \frac{\Delta P^2}{2}\right] + \frac{f_B^2 \Delta P^2}{2}\delta(\omega - \omega_0) \tag{6.2}$$

When the modulating probability $\Delta P \ll 1$, then Equation (6.2) can be approximated as

$$S(\omega) = 2f_B[P_0(1-P_0)] + \frac{f_B^2 \Delta P^2}{2}\delta(\omega - \omega_0) \tag{6.3}$$

36

The first term of the right-hand side of the equation is the quantization noise power of the output of the comparator as it samples its own thermal noise. The second term is the power in the output of the comparator due to the modulating (input) sinewave. Suppose that we integrate the white noise power [the first term of the right-hand side of Equation (6.3)] over the interval $[\omega_0 - \Delta B/2, \omega_0 + \Delta B/2]$, where ΔB is the measurement bandwidth. The minimum detectable modulating sinewave can be defined as the minimum ΔP required to make the integrated noise power in this interval equal to the output power associated with the modulating signal. Experimentally, these quantities will be equal when the power in this interval of width ΔB is 3 dB larger than the magnitude in adjacent intervals of width ΔB (where no modulating signal is present). This factor of 3 dB results from the fact that the white noise and the sinewave add incoherently, so that their magnitude is equal when the noise floor in that bin is raised by 3 dB. So, the minimal detectable signal occurs when the power in the first term of the right-hand side of Equation (6.3) integrated over a bandwidth ΔB is equal to the power in the second term:

$$2f_B P_0(1 - P_0)\Delta B = \frac{f_B^2(\Delta P_{3dB})^2}{2} \tag{6.4}$$

For a comparator with a gray-zone slope dP/dI, we note that

$$I_{3dB} = \frac{\Delta P_{3dB}}{\dfrac{dP}{dI}} \tag{6.5}$$

By substitution of Equation (6.5) into Equation (6.4) and by multiplying both sides by the comparator's small signal input inductance L, we get

$$S_\varepsilon = \Delta E \Delta T = \left[\frac{L(I_{3dB})^2}{2}\right]\frac{1}{\Delta B} = \frac{2P_0(1 - P_0)L}{\left(\dfrac{dP}{dI}\right)^2 f_B} \tag{6.6}$$

Experiments were conducted to measure the power spectral density and the energy sensitivity of a QFP comparator that was clocked at frequencies between 40 Hz and 40 MHz using the experimental setup shown in Figure 6-5. We applied a manually controlled dc input to hold the comparator at the $P_{OUT} = 0.5$ operating point. A clock is used to actuate the QFP comparator, to force it to "make a decision," and to read that decision out to room-temperature electronics. A pulse generator (HP 8082A) is used to generate large-amplitude (~1 V) pulses every time the QFP readout generates a 1. These analog pulses are delivered to the input of an HP dynamic signal analyzer (HP 3561A), which treats the pulse stream as an analog signal. The analyzer bandpass filters the analog signal, resamples it using an A/D converter, and performs an FFT on the sampled data so that the spectral content can be analyzed. The analyzer has the capability of acquiring and averaging the power spectra of a user-specified number of sampled waveforms, and hence an average power spectrum can be obtained.

324151-27
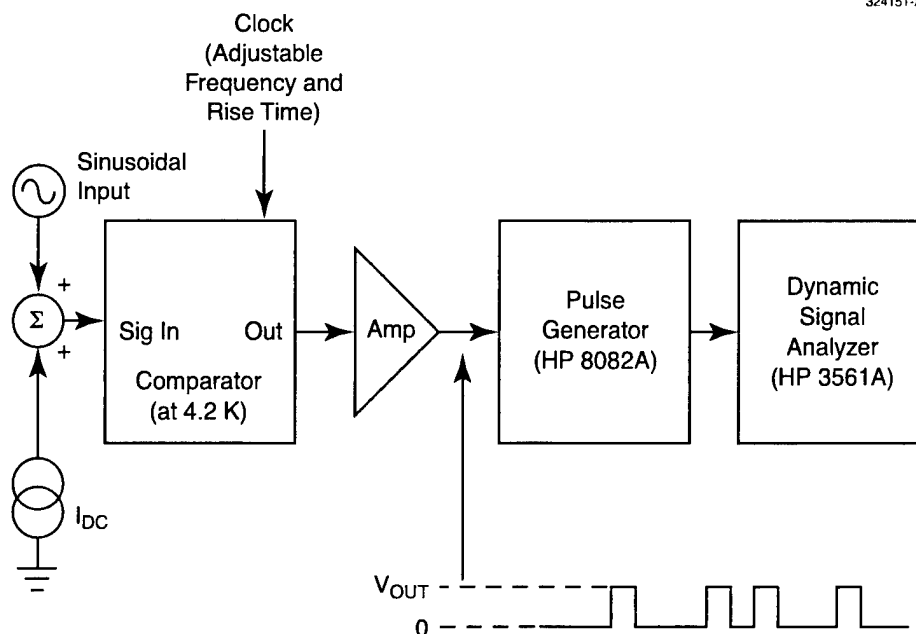
Figure 6-5. Simplified energy sensitivity measurement experiment. An HP signal analyzer is used in place of a digital acquisition system and the computer shown in Figure 6-4. The HP analyzer performs a fast Fourier transform of the analog waveform.

Figure 6-6 shows a typical output from the signal analyzer when a small (~5 nA) 31.0-kHz sinewave was applied to the input of the QFP, and the QFP was biased at its $P_{OUT} = 0.5$ operating point. The QFP was clocked at 40 MHz. In this particular case the analyzer was set to measure the average power spectrum (100 FFT averages) with a center frequency of 31.0 kHz with a resolution of 2.5 Hz. We see over the 1-kHz range of frequencies the noise floor is flat, except at the frequency bin at 31.0 kHz where the input sinusoid is applied. This frequency bin is 10 dB above the noise floor. We adjusted the amplitude of the applied input current (flux) so that the 31.0-kHz frequency bin was 3 dB above the noise floor. We could then establish the sensitivity of the comparator.

We also examined the spectrum from dc to 10 kHz in 25-Hz bin sizes, and we noted that the noise floor was flat, except at a few integer multiples of 60 Hz, where noise spikes were observed. We suspect that the observed 60-Hz noise comes from pickup of line voltages into the output of the pulse generator and is not pickup which is present in the input waveform. When we measured the amplitude of the noise floor from dc to 10 Hz in 25-mHz steps, we observed that the floor began to rise below about 5 Hz. This low-frequency excess noise is due either to the excess noise that is found in the junctions of the comparator

38
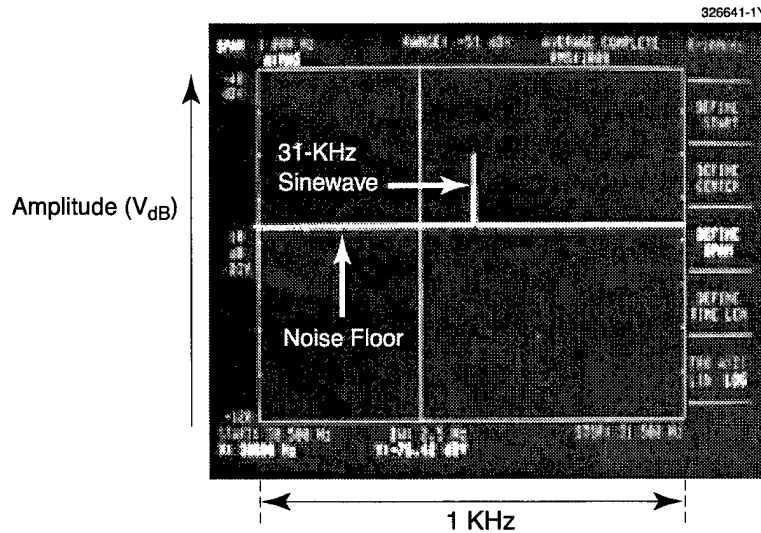
Figure 6-6. Typical output of HP signal analyzer. A 31-kHz sinewave is applied to the input of the QFP comparator. The noise floor is flat except at the input frequency. The signal amplitude at which the signal is 3 dB above the noise floor can be measured, and the energy sensitivity can thus be computed.

[13] or to low-frequency noise from our dc biasing apparatus. We also measured the magnitude of the noise floor, and we found it to be inversely proportional to the clock frequency from 40 Hz to 40 MHz as we expected. The margins in our readout circuit limited us to 40 MHz operation, and we are redesigning the readout circuit so that it will operate well above 1 GHz.

By using the experimental setup shown in Figure 6-5 we have computed the energy sensitivity of the QFP comparator at various clock frequencies with different clock rise times by measuring the slope of the gray zone dP/dI and by measuring the minimum detectable signal [refer to Equation (6.6)]. The reader should refer to [7] to understand the relationship between clock rise time and the gray-zone slope for the QFP comparator. We have biased the comparator at its maximum gray-zone slope with $P_{OUT} = 0.5$. The comparator's small signal input inductance was estimated to be 4.0 pH. In each case the bin width ΔB was chosen to be 2.5 Hz, and we arbitrarily chose 31.0 kHz to be the frequency at which the I_{3dB} measurements were made. We note for shorter clock rise times the slope dP/dI is decreased, and hence S_ε is larger. Thus the comparator is less sensitive. The energy sensitivity calculations based on the minimum detectable signal amplitude and based on the slope of the gray zone (dP/dI) are plotted in Figure 6-7. Sensitivity values derived by the minimum-detectable-sinewave method are shown as squares, and those determined by gray-zone measurements are represented by crosses. The sensitivity values based on the two measurements are in agreement to within a factor of 2. The solid lines are projections of the energy sensitivity for constant exciter rise times (constant values of dP/dI) but for varied clock frequencies. The right sides of the
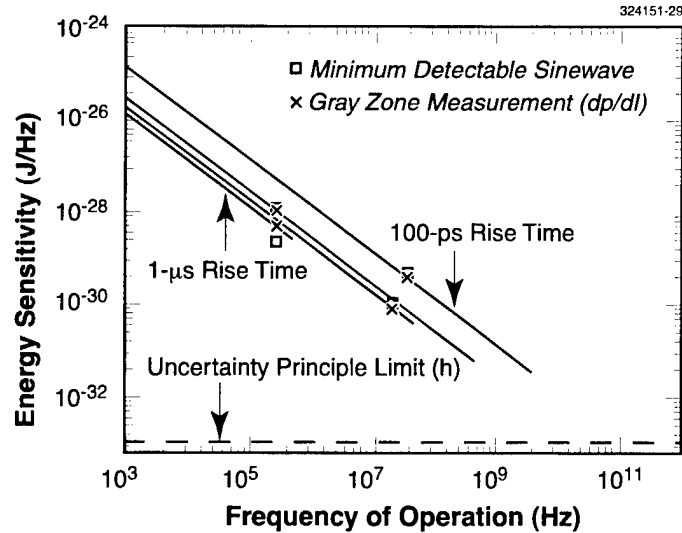
Figure 6-7. Plot of energy sensitivity computed by two methods: using method of minimum detectable signal (squares), and using gray-zone (dP/dI) method (crosses). Measurements were made at three different clock frequencies and with four different clock rise times. Lines represent projections of energy sensitivity for constant exciter rise times (constant values of dP/dI) but for varied clock frequencies.

lines end at the highest possible clock frequency for the given exciter rise time. The value at which the energy sensitivity is best, when S_E is at a minimum, is shown on the graph as the uncertainty-principle limit (h). This is the approximate limit at which the ultimate sensitivity has been reached. We believe with better comparator designs the slope dP/dI can be increased for a given clock rise time, and hence the sensitivities in Figure 6-7 can be improved for the given clock speeds and clock rise times. As we operate comparators beyond gigahertz speeds it will be important from an applications standpoint to establish (1) whether or not the noise floor will remain white across a frequency range at which the circuit is clocked and (2) whether the energy sensitivity S_E can approach $S_E = h$, the uncertainty principle limit.

<div align="right">

D. A. Feld   J. P. Sage

K. K. Berggren   A. Siddiqui

</div>

REFERENCES

1. Solid State Research Report, Lincoln Laboratory, MIT, 1994:4, p. 33.

2. V. K. Seminov, Y. A. Polyakov, and D. Schneider, extended abstracts of ISEC, 1997, p. 41.

3. S. V. Rylov and R. P. Robertazzi, *IEEE Trans. Appl. Supercond.* **5**, 2260 (1995).

4. D. L. Miller, J. X. Przybysz, A. H. Worsham, and A. Miklich, extended abstracts of ISEC, 1997, p. 38.

5. V. K. Semenov, T. V. Fillipov, Y. A. Polonsky, and K. K. Likarev, *IEEE Trans. Appl. Supercond.* **7**, 3617 (1997).

6. T. Fillipov, Y. A. Polyakov, V. K. Semenov, and K. K. Likharev, *IEEE Trans. Appl. Supercond.* **7**, 2240 (1995).

7. H. Ko and G. Lee, *IEEE Trans. Appl. Supercond.* **2**, 156 (1992).

8. M. Radparvar and S.V. Rylov, *IEEE Trans. Appl. Supercond.* **7**, 3682 (1997).

9. N. Fujimaki, H. Tamura, T. Imamura, and S. Hasuo, *IEEE Trans. Appl. Supercond.* **35**, 2412 (1988).

10. N. Fujimaki, K. Gotoh, T. Imamura, and S. Hasuo, *J. Appl. Phys.* **7**, 6182 (1992).

11. U. Faith, R. Hundhausen, T. Fregin, P. Gerigk, and W. Eschner, *IEEE Trans. Appl. Supercond.* **7**, 2747 (1997).

12. N. Fujimaki, H. Tamura, T. Imamura, and S. Hasuo, *J. Appl. Phys.* **65**, 1626 (1989).

13. C. T. Rogers and R. A. Buhrman, *IEEE Trans. Appl. Magn.* **Mag-19**, 453 (1983).

7. ADVANCED SILICON TECHNOLOGY

7.1 HIGH-FREQUENCY PERFORMANCE OF A FULLY DEPLETED 0.25-μm SOI CMOS TECHNOLOGY

A fully depleted (FD) 0.25-μm silicon-on-insulator (SOI) CMOS process technology has been developed and established at Lincoln Laboratory. FDSOI technology allows a significant reduction of the dynamic power consumption of large digital circuits, thanks to reduced junction capacitances and low supply voltage operation [1]. Moreover, SOI substrates offer the capability to integrate passive elements with high-frequency metal-oxide semiconductor field-effect transistors (MOSFETs) to produce high-performance circuits operating in the microwave range. These advantages over bulk technologies provide a wide variety of potential applications for SOI, particularly in the area of mixed-signal integrated circuits where high-performance digital circuits can be combined with high-frequency rf receivers or analog devices on a single chip. This FDSOI CMOS technology has previously demonstrated impressive performance with 25-ps delay per ring oscillator stage and 40-fJ energy per transition having been achieved for the 0.25-μm technology [1]. Here, we report the high-frequency performance of both n- and p-channel 0.25-μm MOSFETs for the baseline FDSOI CMOS process technology.

On-wafer microwave measurements were performed on a number of 0.25-μm MOSFETs fabricated during Lincoln Laboratory's multiuser fabrication runs. Specifically, two-port small-signal S-parameter measurements were made on both n- and p-channel devices from 1 to 21 GHz using an HP 8510 network analyzer and Cascade probes. Cascade probe calibration was performed both off and on chip, but no attempt was made to de-embed the device parasitics associated with the contact pads. Figure 7-1 shows an n-channel MOSFET device layout suitable for common-source mode Cascade probe measurements. Maximum stable gain, maximum available gain, and short-circuit current gain (h_{21}) can be calculated from the measured S-parameter data, and both F_t and F_{max} can be determined from appropriate extrapolations to the unity gain frequency. Figures 7-2 through 7-4 display gain vs frequency curves for three 0.25-μm gate length MOSFETs, one p-channel and two n-channel devices. F_t near 30 GHz and F_{max} in the range 30–40 GHz (estimated conservatively) were obtained for the n-channel FETs. These results are state of the art for 0.25-μm FDSOI CMOS technology. The p-channel device yielded an F_t of 13 GHz and an F_{max} near 20 GHz, as seen in Figure 7-3.

It should be pointed out that these devices were fabricated from the baseline digital CMOS process, and no attempt was made to further optimize the devices for rf performance. The impressive performance is due to a combination of the silicided source, gate, and drain contact technologies, which have resulted in relatively low series (including contact) and gate resistances for the devices, and the multi-gate-finger device design. Of additional interest is the fact that Figure 7-2 displays the rf results for a device fabricated during the first multiuser process run, while Figure 7-4 displays equivalent results for an n-channel device fabricated during the second multiuser run. The two devices, while having nominally the same channel length, differ in two significant ways: device layout and threshold voltage. The device of Figure 7-4 has a higher threshold voltage which results in much lower drain current and transconductance compared to the

324151-30
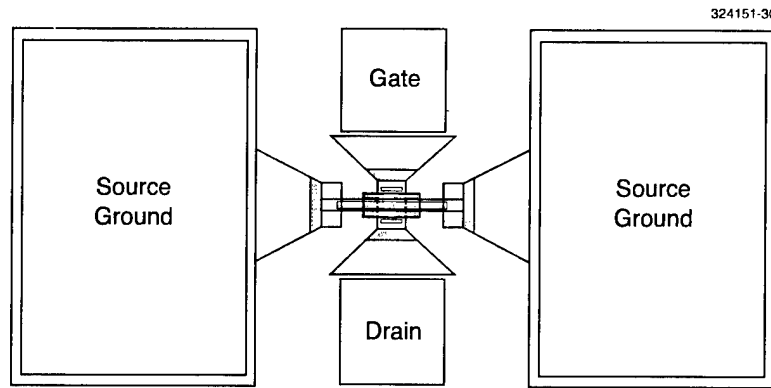
(a)
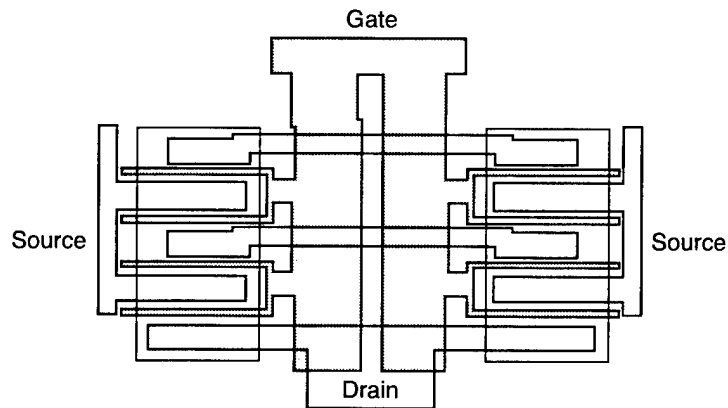
(b)

Figure 7-1. (a) Cascade probe device layout for the 0.25-μm n-channel MOSFET showing source, gate, and drain regions and contact pads suitable for common or grounded source S-parameter measurements. (b) Closeup showing the multifinger gate design. Total gate width of the device is 8 × 5 μm = 40 μm.
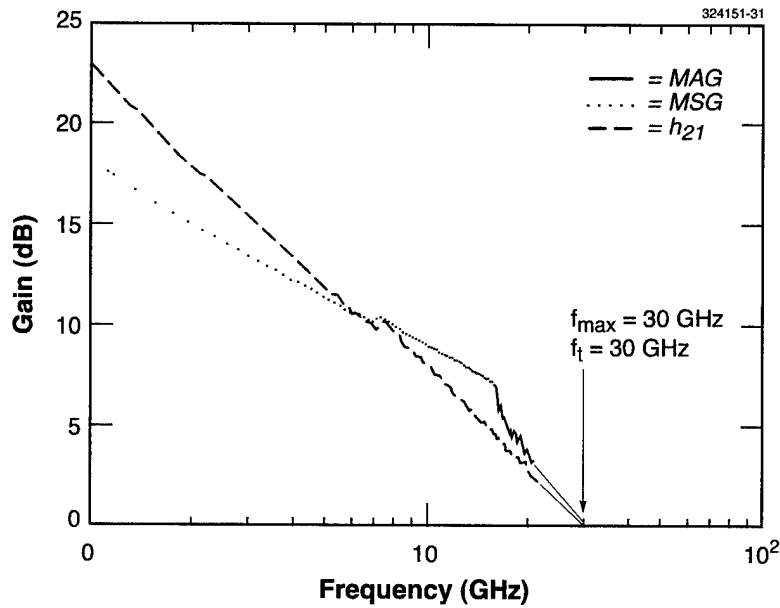
Figure 7-2. The h_{21}, *maximum available gain (MAG), and maximum stable gain (MSG) as function of frequency calculated from two-port S-parameter measurements made on 0.25-μm n-channel MOSFET fabricated from multiuser project run 1. Both* F_t *and* F_{max} *are approximately 30 GHz.*
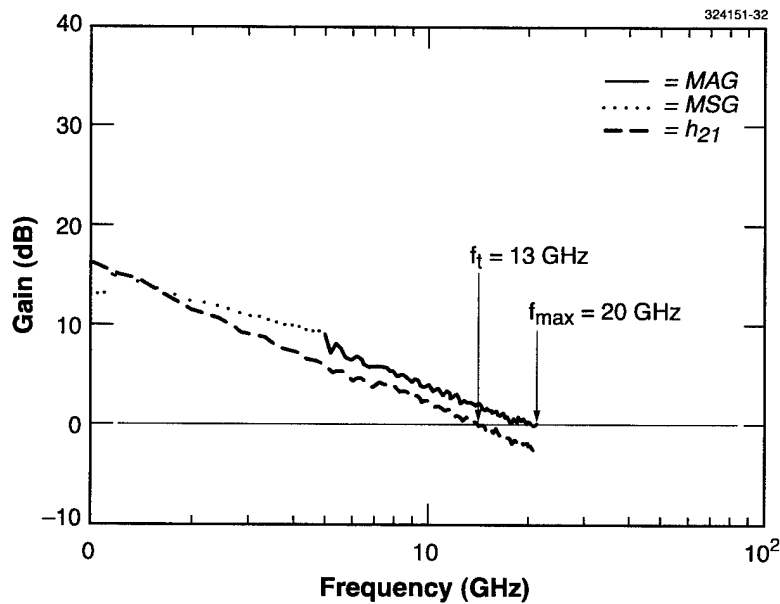
Figure 7-3. The h_{21}, *MAG, and MSG vs frequency calculated from two-port S-parameter measurements made on a 0.25-μm p-channel MOSFET fabricated from multiuser project run 1.* F_t *and* F_{max} *are 13 and 20 GHz, respectively.*

45
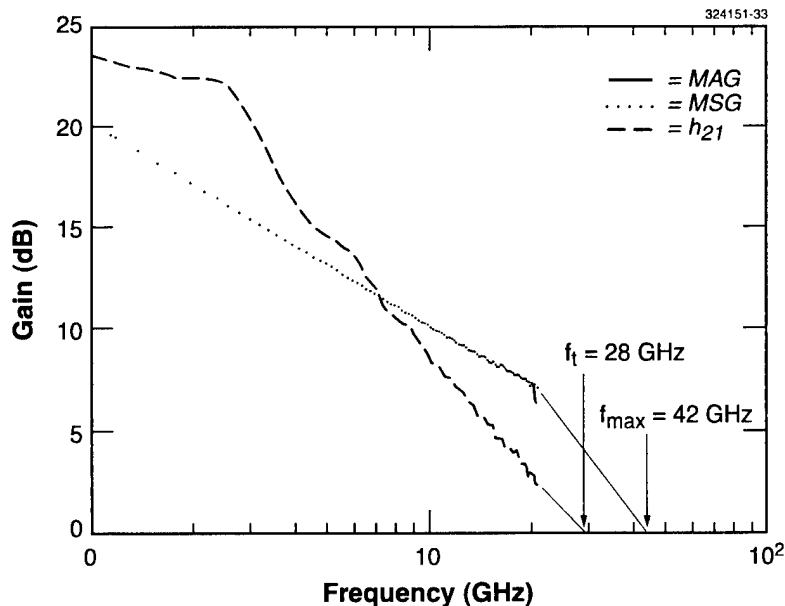
Figure 7-4. The h_{21}, MAG, and MSG vs frequency calculated from two-port S-parameter measurements for a 0.25-μm n-channel MOSFET fabricated from multiuser project run 2. F_t and F_{max} are 28 and 42 GHz, respectively.

device of Figure 7-2. However, this device layout uses a much smaller gate pad in its rf design which results in much lower parasitic capacitance compared to the device of Figure 7-2. The two effects essentially cancel each other such that both devices have F_t's near 30 GHz. However, it does suggest that the optimum combination of device design and threshold voltage should yield F_t's somewhat higher, perhaps near 40 GHz, even for the current 0.25-μm baseline process. Further aggressive scaling to 0.1-μm gate length for *n*-channel MOSFETs could yield F_t's near 100 GHz, provided series resistance effects can be minimized.

D. D. Rathman
C. L. Chen
R. H. Mathews

REFERENCE

1.   Solid State Research Report, Lincoln Laboratory, MIT, 1997:3, p. 39.

REPORT DOCUMENTATION PAGE

Form Approved
OMB No. 0704-0188

1. AGENCY USE ONLY (*Leave blank*)	2. REPORT DATE 15 November 1998	3. REPORT TYPE AND DATES COVERED Quarterly Technical Report, 1 August–31 October 1998

4. TITLE AND SUBTITLE

Solid State Research

5. FUNDING NUMBERS

C — F19628-95-C-0002

6. AUTHOR(S)

David C. Shaver

7. PERFORMING ORGANIZATION NAME(S) AND ADDRESS(ES)

Lincoln Laboratory, MIT
244 Wood Street
Lexington, MA 02420-9108

8. PERFORMING ORGANIZATION REPORT NUMBER

1998:4

9. SPONSORING/MONITORING AGENCY NAME(S) AND ADDRESS(ES)

HQ Air Force Materiel Command
AFMC/STSC
Wright-Patterson AFB, OH 45433-5001

10. SPONSORING/MONITORING AGENCY REPORT NUMBER

ESC-TR-98-044

11. SUPPLEMENTARY NOTES

None

12a. DISTRIBUTION/AVAILABILITY STATEMENT

Approved for public release; distribution is unlimited.

12b. DISTRIBUTION CODE

13. ABSTRACT (*Maximum 200 words*)

This report covers in detail the research work of the Solid State Division at Lincoln Laboratory for the period 1 August–31 October 1998. The topics covered are Quantum Electronics, Electro-optical Materials and Devices, Submicrometer Technology, Biosensor and Molecular Technologies, Microelectronics, Analog Device Technology, and Advanced Silicon Technology. Funding is provided by several DoD organizations — including the Air Force, Army, BMDO, DARPA, Navy, NSA, and OSD — and also by the DOE, NASA, and NIST.

14. SUBJECT TERMS

quantum electronics	biosensor technology	yttrium aluminum garnet	bioelectronic sensor
electro-optical devices	microelectronics	epitaxial growth	curved focal plane
materials research	analog device technology	tunable fiberring laser	superconductive comparator
submicrometer technology	advanced silicon technology	resist outgassing	

15. NUMBER OF PAGES

66

16. PRICE CODE

17. SECURITY CLASSIFICATION OF REPORT	18. SECURITY CLASSIFICATION OF THIS PAGE	19. SECURITY CLASSIFICATION OF ABSTRACT	20. LIMITATION OF ABSTRACT
Unclassified	Same as Report	Same as Report	Same as Report